

Trace-Norm Adversarial Examples

Ehsan Kazemi¹, Thomas Kerdreux^{2,3}, and Liqiang Wang¹

¹Department of Computer Science, University of Central Florida, Florida, USA.

²D.I., UMR 8548, École Normale Supérieure, Paris, France.

³INRIA, Paris, France

July 6, 2020

Abstract

White box adversarial perturbations are sought via iterative optimization algorithms most often minimizing an adversarial loss on a ℓ_p neighborhood of the original image, the so-called distortion set. Constraining the adversarial search with different norms results in disparately structured adversarial examples. Here we explore several distortion sets with structure-enhancing algorithms. These new structures for adversarial examples, yet pervasive in optimization, are for instance a challenge for adversarial theoretical certification which again provides only ℓ_p certificates. Because adversarial robustness is still an empirical field, defense mechanisms should also reasonably be evaluated against differently structured attacks. Besides, these structured adversarial perturbations may allow for larger distortions size than their ℓ_p counter-part while remaining imperceptible or perceptible as natural slight distortions of the image. Finally, they allow some control on the *generation* of the adversarial perturbation, like (localized) bluriness.

1 Introduction

Adversarial examples are inputs to machine learning classifiers designed to cause the model to misclassify. These are searched in the vicinity of some dataset samples, typically in their norm-ball neighborhoods, the so-called *distortion set*. When replacing every test set samples with their associated sought for adversarial examples, the accuracy of classically trained classifiers quickly drops to zero as a function of the considered norm-ball radius. This lack of robustness challenges the security of some real-world systems as well as questions the neural classifiers generalizing properties [Schmidt et al., 2018, Stutz et al., 2019].

This has hence sired a series of works proposing attacks or defenses methods (both practical or theoretical). Most of the attack and defense mechanisms considered ℓ_p neighborhoods. While some recent papers [Xu et al., 2018, Wong et al., 2019] pointed out the benefits of other families of distortions sets, as well as others, outlined the inherent limitations of the ℓ_p balls [Sharif et al., 2018, Sen et al., 2019], many classical norm families remained mostly unexplored in the adversarial setting.

In the white-box framework, the attacker has access to backward passes on the model. Adversarial examples are then iterates of optimization algorithms that seek to minimize constrained adversarial losses. Although norms are equivalent in the image finite-dimensional space, the type of norm-ball influences the structure of the optimization algorithm iterates as well as the (local) minima to which they seek to converge. In such an empirical field, it is hence essential to explore the effect of particular structures in adversarial perturbation besides ℓ_p balls, see Figure 1 for an example.

For instance, it may perfectly be that some empirical defense mechanisms leverage on the lack of a certain pattern in the adversarial perturbation. Providing a catalog of many structured attacks would then at least warn us against such a possibility.

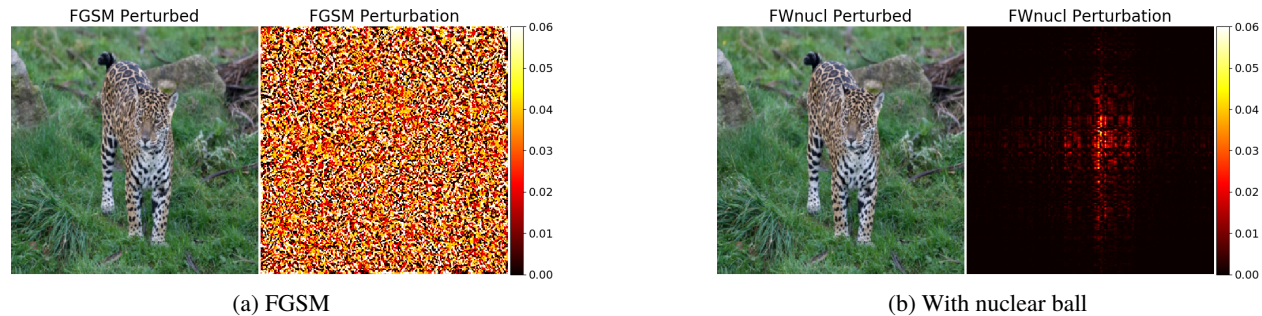


Figure 1: The images correspond to two types of targeted attacks. Projected Gradient Descent (PGD) solve (1) constrained by a ℓ_∞ ball while FWnucl solves (1) constrained with a nuclear ball. The type of adversarial perturbations differs significantly in structure.

The radius of the convex balls is often taken small enough to ensure that the adversarial perturbations are imperceptible. This imperceptibility requirement is pervasive in the literature, although it is far from being the only regime for adversarial examples [Gilmer et al., 2018, §2] leading to security issues. Adversarial examples also challenge the generalization properties of classifiers. However, the imperceptibility of the distortion does not play a special role in that respect, especially when the ideal level of perturbation is arguably the one that guarantees that the labeled content of the original image is preserved (for a human observer) in the adversarially perturbed image. Actually, the imperceptible deformation regime of non-robust classifiers has arguably received much attention because it *highlights the limitation of the analogy between human perception and the processing done by machine learning systems* [Gilmer et al., 2018]. Not being able to overcome this issue would then challenge the belief that current neural networks are possible models of some biological brains.

Here, we do not limit ourselves to the imperceptible regime of perturbation. Instead, we explore adversarial examples’ structure leading to possibly perceptible deformations that would yet be considered as *non-suspicious* alteration of the image. For instance, the nuclear ball, which is the convex relaxation of matrix rank, qualitatively leads to blurred versions of the initial image. This blurring effect could be easily localized to specific semantic areas in the image simply by considering the group-nuclear ball distortion set, where the groups are defined accordingly.

For the sake of simplicity, we focus on un-targeted adversarial examples via the classical optimization approach with respect to x

$$\begin{aligned} & \text{minimize} && L(f(x), t) \\ & \text{subject to} && \|x - x^{ori}\| \leq \epsilon \end{aligned}$$

where L is an adversarial loss, f the neural classifier and t a label different from the label of the original image x_{ori} .

Related Work. Several works question the reason for considering ℓ_p neighborhood as distortion sets and propose other models and methods. For instance, Sharif et al. [2018] suggest that ℓ_p norms are neither the right metric for perceptually nor even content-preserving adversarial examples. Sen et al. [2019] show on a behavioral study that that ℓ_p norms and some other metrics do not fit with human perception.

Others consider adversarial perturbations beyond the ℓ_p distortion sets. Engstrom et al. [2017] show that simple rotation and translation can be efficient adversarial methods. Xu et al. [2018] consider group-lasso

distortion sets to better interpret some adversarial example properties, solving the optimization problem via ADMM. Liu et al. [2018] generate adversarial examples based on the geometry and physical rendering of the image. They notably suggest that *large pixel perturbations can be realistic if the perturbation is conducted in the physical parameter space (e.g., lighting)*. [Wong et al., 2019] recently argue that robustness to Wasserstein perturbations of the original image is essentially an invariance that should typically exist in classifiers.

Some methods solve the adversarial optimization problem on subspaces, which might lead to specifically structured adversarial examples. While random subspace [Yan et al., 2019] does not induce specific perturbation structure, projection on low-frequency domain [Guo et al., 2018] or onto the subspace generated by the top few singular vectors of the image [Yang et al., 2019, §3.4.] do induce structured adversarial examples. These approaches aim at reducing the search space of adversarial perturbation for computational reasons.

Finally, one can consider the problem of adversarial attack generation as an image processing task. A recent trend to various types of such algorithms, like in conditional or unconditional GAN, style transfer algorithms, or image translation algorithms, has been to provide more control for the user of the modified or generated images [Reed et al., 2016, Gatys et al., 2017, Risser et al., 2017, Lu et al., 2017]. Providing a little more control to the attacker on the generated type of adversarial perturbations stands in that line of works.

Contribution. We study some families of structured norms in the adversarial example setting. This is a pretense to more generally motivate the relevance of structured attacks (*i.e.* besides the ℓ_p distortion set), that are largely unexplored. For instance, it challenges the theoretical certification approaches that are stated in terms of ℓ_p neighborhoods. It is also a versatile approach to produce specific modification of the adversarial images, like (local) blurriness.

Outline. In Section 2 we motivate simple families of norm resulting in structured adversarial perturbations which can then be leveraged for crafting specific adversarial attacks. In Section 3 we use the conditional gradient algorithms designed to efficiently solve (1) under the various considered structured norms and we then report some numerical experiments in Section 4.

2 Structured Distortion Sets

Here we detail some simple structured families of norms that, to the best of our knowledge, have not yet been explored in the context of adversarial attacks. When solving (1), these lead to specific structures in the outputs, giving some control, for instance to a potential attacker, on the way the adversarial perturbation alters the test sample images. In addition, these perturbations can be further adapted to the attacked image by solving the adversarial problem (1) with a group-norm distortion sets, where the groups are adapted to the image.

In Section 3, we seek to solve the optimization problem (1) with conditional gradient algorithms. When applicable, this ensures that the early algorithms’ iterates have a specific structure. Indeed, each iteration of these algorithms requires to solve a Linear Minimization Oracle (LMO). For a direction d and a convex set \mathcal{C} , it is defined as

$$\text{LMO}_{\mathcal{C}}(d) \in \underset{v \in \mathcal{C}}{\text{argmin}} d^T v. \quad (3)$$

The iterates of conditional gradient algorithms are then constructed as (sparse) convex combination of such solutions. These can always be chosen as extreme points of \mathcal{C} . Hence, the specific structure of the solutions of the LMO is then passed on to the early optimization iterates. In Section 2.2, we review how to leverage on weighted group norms in order to localize the low-rank perturbations.

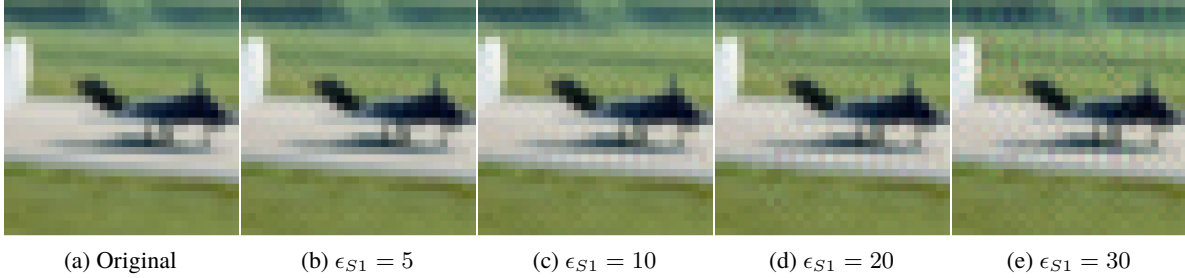


Figure 2: For a test image of CIFAR-10, we computed the various adversarial examples stemming from solving (1) on the nuclear ball with Frank-Wolfe algorithm. From left to right: original image, adversarial example with a nuclear radius of $\epsilon_{S1} = 5, 10, 20, 30$. Note that the adversarial examples are already miss-classified with $\epsilon_{S1} = 3$; here we increase the radius purposely to observe the perturbation on the initial image.

2.1 Low-rank perturbation

We write $\|\cdot\|_{S1}$ for the nuclear norm, the sum of the matrix singular value, a.k.a. the trace norm or the 1-Schatten norm. The nuclear norm has been classically used to promote low-rank solutions of convex optimization problems [Fazel et al., 2001, Candès and Recht, 2009] such as matrix completion. Here, we propose to simply consider nuclear balls as distortion sets when searching for adversarial examples in problem (1). We later explore the various benefit of using this structure. To our knowledge, the low-rank structure is used in different aspects of some defense techniques but not for adversarial attacks. As an empirical defense mechanism, Langeberg et al. [2019] add a penalization in the training loss that promotes the low-rank structure of the convolutional layers filters. Yang et al. [2019] notably propose a pre-processing of the classifier outputs, which randomly removes some input pixels and further reconstructs it via matrix completion. We hence seek to solve the following optimization problem

$$\operatorname{argmin}_{\|x-x^{ori}\|_{S1} \leq \epsilon} L(f(x), t).$$

This is just one example among the family of p -Schatten norms $\|\cdot\|_{Sp}$, the p -norm of the singular value vector. These lead to differently structured adversarial examples and may be interesting to defeat certification approaches that are stated in terms of ℓ_p neighborhoods. The LMO (3) for a nuclear ball of radius ρ is given as

$$\operatorname{LMO}_{\|\cdot\|_{S1} \leq \rho}(M) \triangleq \rho U_1 V_1^T,$$

when the singular decomposition of the matrix M is USV^T . The computation of the LMO involves U_1 and V_1 , i.e., the right and left singular vectors associated to the largest singular value ρ . Others optimization approaches like PGD, would require the knowledge of the full SVD at each iteration. Note that for q -Schatten norm (with $q > 1$) the LMO is also explicit and involve the full singular decomposition (see [Garber and Hazan, 2015, Lemma 7] for instance).

Finally, we observe that, in practice, the adversarial perturbations add a blurring effect to the initial images, see Figure 2 for instance. In some potential security scenarios, such perturbations could then be perceived as simple alterations of the image rather than a malware deformation of it, hence not raising the human attention (see [Gilmer et al., 2018] for real-world scenarios).

2.2 Group constraints

We now propose group-norms that depend on a partition of the pixels' coordinates into groups. For instance, such a partition can be adapted from a segmentation of the sample image. These group-norms are a

combination of two norms: a local one applied on vectors formed by each group of pixels' values, and a global one applied on the vectors of the norms of all the groups. Here, we consider the nuclear norm as the local norm and the global ℓ_1 norm to induce sparsity at the group level. Considering such norms allows to constrain the type of perturbations further.

Note here that our approach is not the only way to produce structured adversarial perturbations. However, Conditional Gradient iterates (see Section 3) are all structured according to the structured norm ball with no other algorithmic modification than the knowledge of the LMO. We can hence easily explore structures in adversarial examples implementing a trade-off between decrease the adversarial loss and enforcing specific structures to the perturbation.

Nuclear Group Norm. Let \mathcal{G} be an ensemble of groups of pixels' coordinates of the tensor image of (c, h, w) . Each element $g \in \mathcal{G}$ is a set of pixel coordinates'. Then for $x \in \mathbb{R}^{c \times h \times w}$ we write, with $p \in [1, \infty[\cup\{\infty\}]$,

$$\|x\|_{\mathcal{G},1,p} = \sum_{g \in \mathcal{G}} \|x[g]\|_{S(1)},$$

for the \mathcal{G} -nuclear group-norm, see for instance [Tomioka and Suzuki, 2013]. When \mathcal{G} is a partition of the pixels, $\|\cdot\|_{\mathcal{G},1,S(1)}$ is a norm. The nuclear group-norm allows to localize the blurring effect of the nuclear norm. Indeed, the LMO of \mathcal{G} -nuclear group-norm is given by

$$\text{LMO}_{\|\cdot\|_{\mathcal{G},1,S(1)} \leq \rho}(M) \triangleq \begin{cases} \rho U_1^{(g^*)} (V_1^{(g^*)})^T & \\ 0 & \text{otherwise} \end{cases}, \quad (4)$$

where $g^* = \underset{g \in \mathcal{G}}{\text{argmax}} \|M[g]\|_{S(1)}$ and the singular value decomposition of $M[g]$ for each group g is given by $U^{(g)} S^{(g)} (V^{(g)})^T$. When solving (1) with such norms, each iteration of the conditional gradient will add to the adversarial perturbation a vertex of the form described by (4), *i.e.* a matrix of rank-one on the rectangle defined by the group of pixels in $g \in \mathcal{G}$.

Different Distortion Radius per Group. When perturbing an image, modification in the pixel regions with high variance are typically harder to perceive than pixels modification in low variance regions. This was leveraged on in [Luo et al., 2018] or in the σ -map of [Croce and Hein, 2019, §2.2.]. Weighted nuclear group norms allow to search adversarial perturbations with different distortion radius across the image. With some $w_g > 0$, the weighted nuclear group norm is defined as

$$\|x\|_{\mathcal{G},1,S(1),w} = \sum_{g \in \mathcal{G}} w_g \|x[g]\|_{S(1)},$$

and the LMO for weighted nuclear group-norm is then obtained as

$$\text{LMO}_{\|\cdot\|_{\mathcal{G},1,S(1),w} \leq \rho}(M) \triangleq \begin{cases} \frac{\rho}{w_{g^*}} U_1^{(g^*)} (V_1^{(g^*)})^T & \text{on group of pixels } g^* \\ 0 & \text{otherwise} \end{cases},$$

where $g^* = \underset{g \in \mathcal{G}}{\text{argmax}} \frac{1}{w_g} \|M[g]\|_{S(1)}$ and the singular value decomposition of $M[g]$ for each group g is given by $U^{(g)} S^{(g)} (V^{(g)})^T$. In particular, this means that the solution corresponding to the group associated with g have a nuclear radius of $\frac{\rho}{w_g}$ and the weights w_g allow to control the distortion in each group of pixels.

Structured Attacks and Certification. Some defense methods aim at certifying that some neural network classifiers are constant in balls around test images [Wong and Kolter, 2017, Raghunathan et al., 2018b,a]. In particular, these methods seek at escaping the cat and mice game between empirical attacks and defenses methods. However, it is not yet clear how these scale to large datasets and neural architectures, for instance, [Raghunathan et al., 2018b] only provide certifiable robustness on MNIST with $\epsilon_{\ell_\infty} = 0.1$.

Besides, these methods guarantee certifiable robustness in terms ℓ_p -norms perturbations. Although norms are equivalents in the finite-dimensional space of images, their guarantee may become shallow under a different measure of the distortion set. This was pointed out with Wasserstein distortion sets in [Wong et al., 2019, §5.3.].

3 Structure Enhancing Algorithm for Adversarial Examples

We apply the Frank-Wolfe algorithms [Frank and Wolfe, 1956], a.k.a. conditional gradient algorithms [Levitin and Polyak, 1966], for problem (1). These algorithms have known a recent revival in constrained optimization problems for machine learning. This is notably due to their low cost computational cost per iterations [Jaggi, 2013] as well as the many related theoretical and practical open questions, like linear convergence on polytopes [Guélat and Marcotte, 1986, Garber and Hazan, 2013a,b, Lacoste-Julien and Jaggi, 2013, 2015], convergence on strongly convex set [Levitin and Polyak, 1966, Demyanov and Rubinov, 1970, Dunn, 1979, Garber and Hazan, 2015] or uniformly convex sets [Kerdreux and d’Aspremont, 2020].

On specific constraint structures, such as the one developed in Section 2, conditional gradient algorithms naturally trade off the convergence accuracy with the structure of the early iterates. Note also that for the case of large-scale nuclear norm regularization in convex optimization, the Frank-Wolfe algorithm has been extensively studied [Jaggi and Sulovský, 2010, Lee et al., 2010, Shalev-Shwartz et al., 2011, Harchaoui et al., 2012, Dudik et al., 2012, Allen-Zhu et al., 2017, Garber et al., 2018]. Many variations [Freund et al., 2017, Cheung and Li, 2017] exist which leverage the facial properties (see [Freund et al., 2017, Theorem 3] or originally from [So, 1990]) of the nuclear ball (which is not a polytope nor a strongly convex set).

Algorithm 1 Vanilla Frank-Wolfe

Input: Original image x_0
for $t = 0, \dots, T$ **do**
 $s_t = \text{LMO}_C(-\nabla f(x_t))$.
 $\gamma_t = \text{LineSearch}(x_t, s_t - x_t)$
 $x_{t+1} = (1 - \gamma_t)x_t + \gamma_t s_t$
end for

For all the distortion set we consider, the LMO is explicit. While we do not focus on computational efficiency, we note that the computation of the LMO has a low computational requirement as opposed to projection based approaches. Indeed it require only the first singular vectors as opposed to proximal steps which require the full SVD. Provided access (when applicable) to an upper-bound L of the adversarial loss Lipschitz constant in (1), we use the short step size rule $\gamma_t = \text{clip}_{[0,1]}(\langle -\nabla f(x_t), s_t - x_t \rangle / L \|s_t - x_t\|^2)$. Chen et al. [2018] consider using zero-order Frank-Wolfe algorithm for solving adversarial problems like (1) but in the black-box setting.

When the objective functions are non-convex, *e.g.* with adversarial losses, injecting noise may be beneficial. For instance, this can be done either via random starts or via randomized block-coordinate methods. With some restriction Kerdreux et al. [2018] propose a version of Frank-Wolfe that solves linear minimization oracles on random subsets of the constraint sets. For the nuclear group norm, the sampling scheme could be done at the group-level. For instance, we consider the nuclear group norm with one group per channel, *i.e.*

$\|x\|_{color,S1} = \sum_{c=1}^3 \|x_c\|_{S1}$ where x_c is one of the image channels. We experiment this approach in Section 4.

Here, we did not consider the constraints that the images iterates should belong to the $[0, 1]^d$ box constraints. Instead, we clamp the last iterate to belong to the box constraints. This does not guarantee the convergence to a saddle point but removes the need to compute the Linear Minimization Oracle over the intersection of two sets, which is non-trivial. We are ultimately interested in the effective success rate of the attack that we explore in the subsequent section.

4 Numerical Experiments

This section aims at evaluating the success rate in different scenarios of adversarial examples stemming from the application of Frank-Wolfe algorithms to the adversarial problem (1) with (group) nuclear balls as distortion sets, which we refer as FWnucl.

Experiments Goal. We tested FWnucl white-box attack against two baselines of defenses for untargeted attacks. The first is Madry et al. [2017], the state-of-the-art defense against white-box attacks. It uses the training images augmented with adversarial perturbations to train the network.

The second one Yang et al. [2019] leverages matrix estimation techniques as a pre-processing step; each image is altered by randomly masking various proportions of the image pixels’ and then reconstructed using matrix estimation. For a given training image, this produces a group of images that are used during training, see [Yang et al., 2019, §2.3.] for more details. This provides a non-differentiable defense technique, *i.e.* a method that cannot be straightforwardly optimized via back-propagation algorithms, and was reported to be robust against methods in [Athalye et al., 2018] by circumventing the obfuscated gradients defenses. Qualitatively it leverages a structural difference between the low-rank structure of natural images and the adversarial perturbations that are not specifically designed to share the same structures. A key motivation of our work then is to propose adversarial examples with specific structures, serving at least as a sanity check for defense approaches in the spirit of [Yang et al., 2019].

We report the attack success rates of FWnucl along with those of classical attack methods like Fast Gradient Sign Method (FGSM) Goodfellow et al. [2014], and Projected Gradient Descent (PGD) Madry et al. [2017], both of which being different methods to solve the same adversarial problem (1) where the distortion set is the ℓ_∞ ball. For each technique, we report accuracy as the percentage of adversarial examples that are classified correctly. These numerical experiments demonstrate that the attack success rates for FWnucl are comparable to the classical ones in an imperceptibility regime while also retaining specific structures in the perturbation.

Experiment settings. We assess accuracy of networks on MNIST and CIFAR-10 testsets. For ImageNet we randomly selected 4000 from the ImageNet validation set that is correctly classified. As classically done in previous works, for MNIST, we use the LeNet model with two convolutional layers similar to Madry et al. [2017] and SmallCNN with four convolutional layers followed by three fully connected layers as in Carlini and Wagner [2017]. For CIFAR-10 dataset we use ResNet-18 and its wide version WideResNet and ResNet-50.

Nuclear Attacks Structures. In MNIST dataset there is no texture besides the digits’ active pixels representing the figures. In particular, attacks that tend to perturb all pixels are not good candidates as they require low distortion parameters to be imperceptible. This is, for instance, the case of the Frank-Wolfe attack with nuclear ball distortion sets. Indeed nuclear adversarial examples perturb nearly all the pixels, with values ranging from 1 to 5 (with respect to 255). This is because at each iteration Frank-Wolfe algorithms add a

Table 1: MNIST and CIFAR-10 extensive white-box attack results. FWnucl 20*: FWnucl with $\epsilon_{S1} = 1$. FWnucl 20+: FWnucl with $\epsilon_{S1} = 3$. On MNIST (resp. CIFAR-10) PGD and FGSM have a total perturbation scale of 76.5/255(0.3) (resp. 8/255 (0.031)), and step size 2.55/255(0.01) (resp. 2/255(0.01)). PGD runs for 20 iterations. We reproduce the ME-Net and Madry defense with same training hyper-parameters.

Network	Training Model	Clean	Accuracy under attack			
			FWnucl 20*	FWnucl 20+	PGD 20	FGSM
MNIST						
LeNET	Madry	98.38	95.26	92.76	95.79	96.59
	ME-Net	99.24	97.63	75.41	74.88	46.18
SmallCNN	Madry	99.12	98.19	96.66	95.77	97.95
	ME-Net	99.42	89.56	78.65	76.84	54.09
CIFAR-10						
ResNet-18	Madry	81.25	44.28	3.06	49.95	55.91
	ME-Net	92.09	29.66	4.01	4.99	44.80
WideResNet	Madry	85.1	43.16	2.82	52.49	59.06
	ME-Net	92.09	40.09	16.04	12.73	59.33
ResNet-50	Madry	87.03	40.97	2.64	53.01	61.44
	ME-Net	92.09	47.66	17.81	9.14	58.51

rank-one matrix to the perturbation. These rank one matrices stem from the right and left singular vector of the initial matrix and generally involve many of the image pixels.

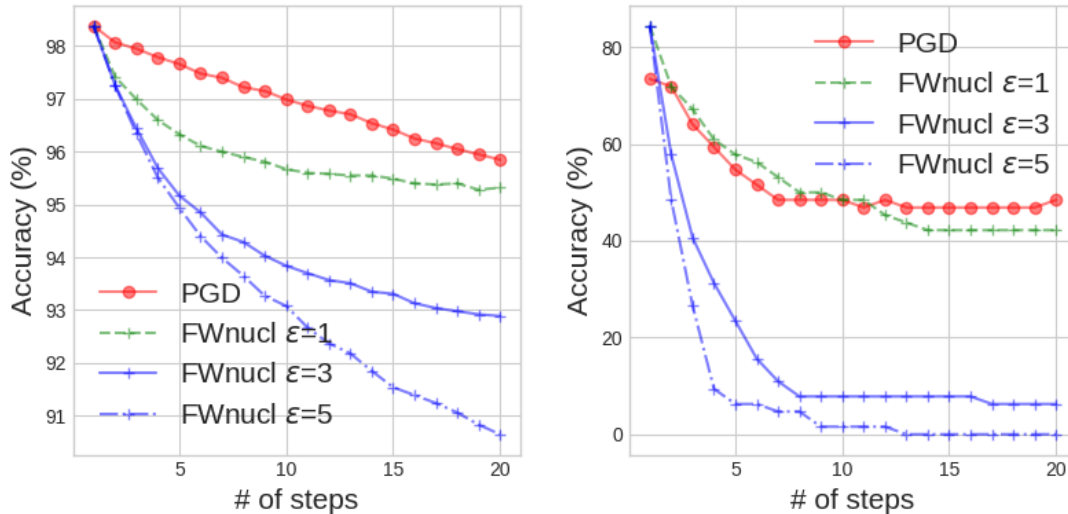
In Table 2 we report the mean ℓ_2 , and nuclear norms of the adversarial noise over all attacks in Table 1 for the CIFAR-10 dataset (see the Appendix for MNIST dataset). Our method with $\epsilon_{S1} = 1$ generates perturbations with almost $7x$ and $10x$ lower ℓ_2 norm for the MNIST dataset. Interestingly, the adversarial examples for FWnucl show significantly lower nuclear norm.

In Figure 3 we report the accuracy of adversarially trained networks over MNIST and CIFAR-10 datasets when attacked with FWnucl. It shows the network’s accuracy at each iteration of a FWnucl attack with various nuclear norm radius $\epsilon_{S1} = 1, 3, 5$.

Figure 4 summarizes the results for FWnucl with varying for standard and robust model on CIFAR-10. The FWnucl algorithm noticeably drops the accuracy rate by increasing the radius ϵ_{S1} . The performance of

Table 2: Comparison of the white-box attacks for CIFAR-10 on ResNet-18 adversarially trained. PGD, on the ℓ_∞ ball, and FGSM have a total perturbation scale of 8/255 (0.031), and step size 2/255(0.01). FWnucl 20*: FWnucl with $\epsilon_{S1} = 1$. FWnucl 20+: FWnucl with $\epsilon_{S1} = 3$.

Attack	ResNet-18		WideResNet		ResNet-50	
	Mean ℓ_2	Mean $\ \cdot\ _{S1}$	Mean ℓ_2	Mean $\ \cdot\ _{S1}$	Mean ℓ_2	Mean $\ \cdot\ _{S1}$
FWnucl 20*	1.38	0.91	1.36	0.90	1.31	0.91
FWnucl 20+	3.37	2.72	3.24	2.62	3.00	2.65
PGD 20	1.68	3.88	1.68	3.97	1.66	3.89
FGSM	1.73	4.04	1.73	4.04	1.73	4.10



(b)

Figure 3: Accuracy of robust models, MNIST (left) and CIFAR-10 (right), versus the number of steps in PGD and FWnucl attacks when varying the nuclear ball radius on the latter.

different FWnucl methods is slightly different, as more FWnucl steps may gain better performances.

Imperceptibility nuclear threshold. We illustrate in Figure 5 some adversarial examples generated by FWnucl, for three different values of epsilon. The imperceptibility threshold depends on the dataset. On CIFAR-10, we qualitatively observed that with $\epsilon_{S1} = 1$, all adversarial examples are perceptually identical to the original images. Also as the dataset becomes more complex, the tolerance of imperceptibility to nuclear ball radius values ϵ_{S1} increases; on ImageNet the imperceptibility threshold is qualitatively for $\epsilon_{S1} = 10$. In Figure 6, we observe that the perturbations are particularly congregated around important regions (i.e., body, head), although there is not a universal configuration to detect specific features that are the most important for the network. While the noise generated by PGD attack exhibits abrupt changes in pixel intensities (see Figure 1), the perturbation from FW has a continuous variations in pixel values. In addition, the number of non-zero pixel values for PGD and FGSM on ImageNet is almost $11x$ and $14x$ larger, respectively than the number of non-zero pixel intensities for FWnucl with $\epsilon_{S1} = 1$.

It is important to characterize the type of deformation that arise with radii above the imperceptibility threshold as the imperceptibility regimes are not the only security scenario. In particular accuracy of robust networks quickly drop to zero in these regimes, see Figure 3-4, facilitating the attacks. In the nuclear ball case, as the radius ϵ_{S1} of the nuclear ball increases, the perturbation becomes perceptible with a blurring effect. Structure in the adversarial examples can be leveraged to create specific perceptible deformation effects that look natural to humans.

Transferability. In Table 3 we investigate the transferability of FWnucl adversarial examples over different architectures for ImageNet. This table shows that there should be some similar structural pattern between independent architectures that FWnucl employs, but the adversaries are mainly network dependent. In Figure 7, we illustrate how the adversarial nuclear structure vary from one network to another for the same image; in particular the perturbation continuously concentrate around the important regions of the image with however varying layout and pattern of perturbation for each network.

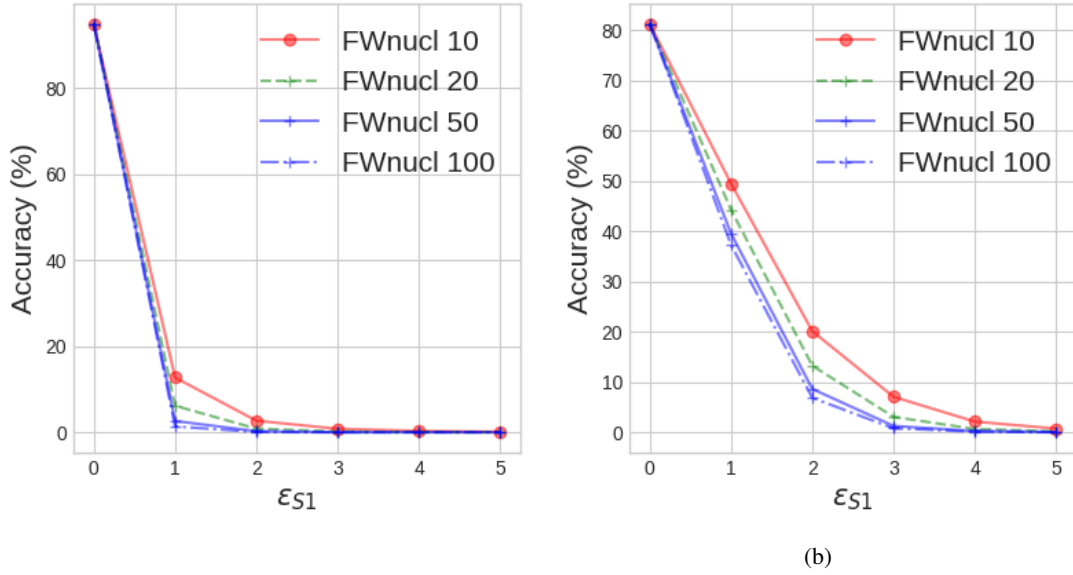


Figure 4: Accuracy of standard model (left) and robust model of Madry (right) on ResNet-18 for CIFAR-10, versus the nuclear ball radius when varying the number of steps.

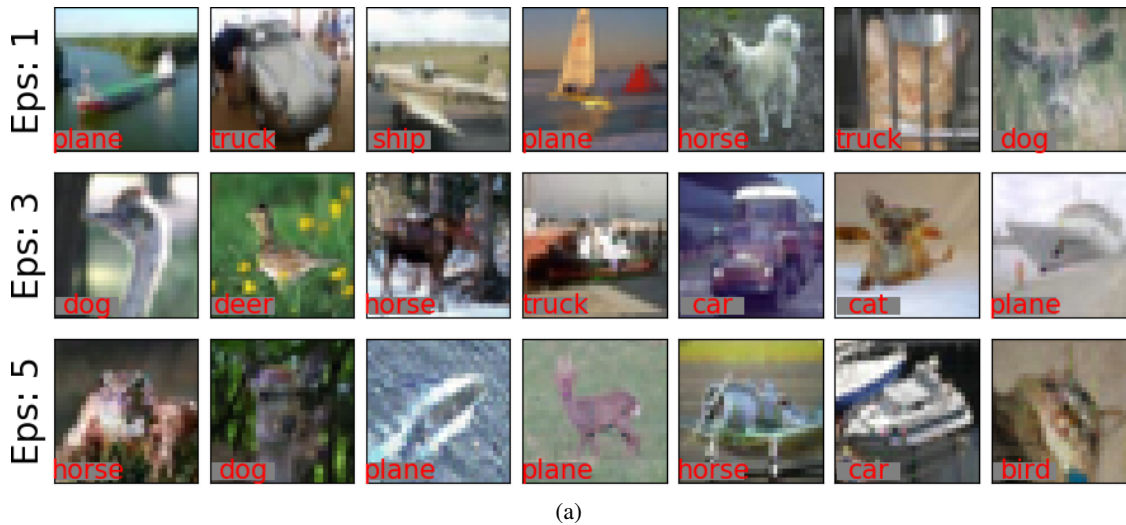


Figure 5: FWnucl adversarial examples for the CIFAR-10 dataset for different radii. The fooling label is shown on the image.

Table 3: Fooling rates of FWnucl adversarial perturbations between several models for 4000 samples from ImageNet. The row indicates the source model and the column indicates the target model.

	ResNet-18	DenseNet121	GoogLeNet
ResNet-18	100	18.15	12.91
DenseNet121	16.56	99.30	11.74
GoogLeNet	15.03	12.37	99.40

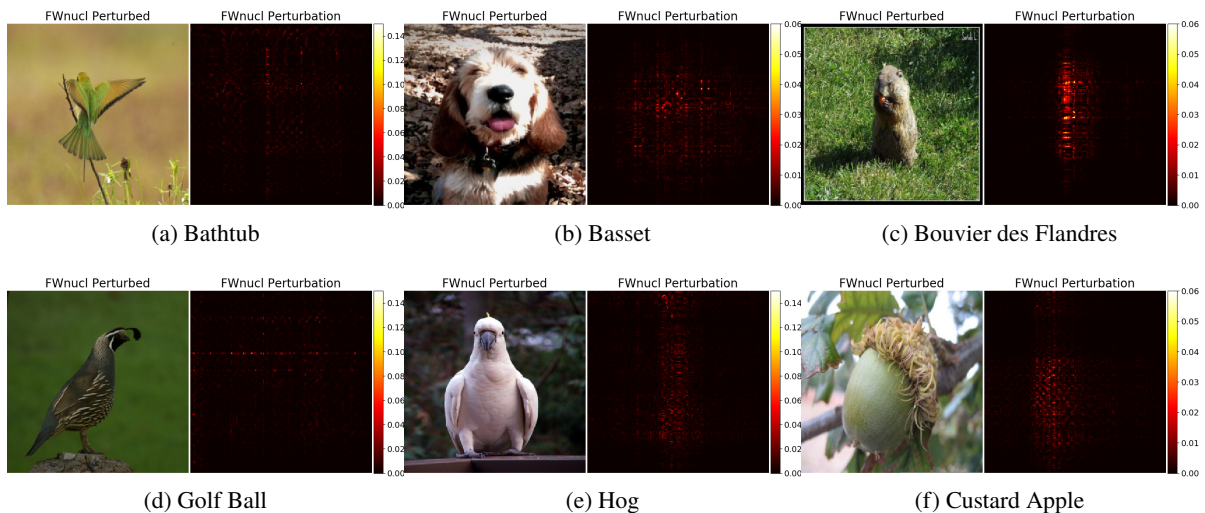


Figure 6: The images display some structural pattern of FWnucl perturbations for the ImageNet dataset on DenseNet121 architecture for various level of distortion, standardly trained. Observe that the adversarial perturbed pixels are accumulated on the areas containing semantic information about the image. FWnucl is conducted with $\epsilon_{S1} = 5$ and 20 iterations.

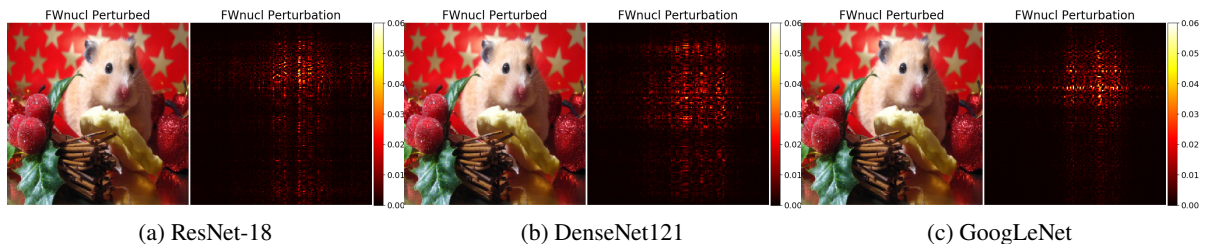


Figure 7: General layout of the FWnucl perturbations for ImageNet across three different architectures.

5 Conclusion

We consider adversarial attacks beyond ℓ_p distortion set. We propose a simple optimization approach producing structured adversarial examples with non- ℓ_p distortion sets. First, it challenges the theoretical certification approaches that so far are given in ℓ_p norm terms. Also, it allows an attacker to design perceptible adversarial examples with specific characteristics, like localized blurriness. Finally, in the imperceptible regime, some defensive pre-processing techniques may rely on a lack of certain patterns in the adversarial perturbations to destroy it. Evaluating robustness against various structured adversarial examples then seems to be a reasonable defense sanity check.

Acknowledgement

T.K. would like to thanks Geoffrey Negiar for interesting discussions on the topic.

References

- Zeyuan Allen-Zhu, Elad Hazan, Wei Hu, and Yuanzhi Li. Linear convergence of a frank-wolfe type algorithm over trace-norm balls. In *Advances in Neural Information Processing Systems*, pages 6191–6200, 2017.
- Pr Massih-Reza Amini, Pr Alexander Nazin, Pr Stéphane Chrétien, Nelly Pustelnik, Pr Joseph Salmon, Pr Anatoli Juditsky, Jérôme Malick, and Pr Zaid Harchaoui. *Nonsmooth Optimization for Statistical Learning with Structured Matrix Regularization*. PhD thesis, University of Washington, 2017.
- Anish Athalye, Nicholas Carlini, and David Wagner. Obfuscated gradients give a false sense of security: Circumventing defenses to adversarial examples. *arXiv preprint arXiv:1802.00420*, 2018.
- Emmanuel J Candès and Benjamin Recht. Exact matrix completion via convex optimization. *Foundations of Computational mathematics*, 9(6):717, 2009.
- Nicholas Carlini and David Wagner. Towards evaluating the robustness of neural networks. In *2017 IEEE Symposium on Security and Privacy (SP)*, pages 39–57. IEEE, 2017.
- Jinghui Chen, Jinfeng Yi, and Quanquan Gu. A frank-wolfe framework for efficient and effective adversarial attacks. *arXiv preprint arXiv:1811.10828*, 2018.
- Edward Cheung and Yuying Li. Projection free rank-drop steps. *arXiv preprint arXiv:1704.04285*, 2017.
- Francesco Croce and Matthias Hein. Sparse and imperceivable adversarial attacks. In *Proceedings of the IEEE International Conference on Computer Vision*, pages 4724–4732, 2019.
- V. F. Demyanov and A. M. Rubinov. Approximate methods in optimization problems. *Modern Analytic and Computational Methods in Science and Mathematics*, 1970.
- Miroslav Dudik, Zaid Harchaoui, and Jérôme Malick. Lifted coordinate descent for learning with trace-norm regularization. In *Artificial Intelligence and Statistics*, pages 327–336, 2012.
- Joseph C Dunn. Rates of convergence for conditional gradient algorithms near singular and nonsingular extremals. *SIAM Journal on Control and Optimization*, 17(2):187–211, 1979.
- Logan Engstrom, Brandon Tran, Dimitris Tsipras, Ludwig Schmidt, and Aleksander Madry. A rotation and a translation suffice: Fooling cnns with simple transformations. *arXiv preprint arXiv:1712.02779*, 2017.
- Maryam Fazel, Haitham Hindi, and Stephen P Boyd. A rank minimization heuristic with application to minimum order system approximation. In *Proceedings of the 2001 American Control Conference.(Cat. No. 01CH37148)*, volume 6, pages 4734–4739. IEEE, 2001.
- Marguerite Frank and Philip Wolfe. An algorithm for quadratic programming. *Naval research logistics quarterly*, 3(1-2):95–110, 1956.
- Robert M Freund, Paul Grigas, and Rahul Mazumder. An extended frank-wolfe method with “in-face” directions, and its application to low-rank matrix completion. *SIAM Journal on Optimization*, 27(1): 319–346, 2017.

- Dan Garber and Elad Hazan. A linearly convergent conditional gradient algorithm with applications to online and stochastic optimization. *arXiv preprint arXiv:1301.4666*, 2013a.
- Dan Garber and Elad Hazan. Playing non-linear games with linear oracles. In *2013 IEEE 54th Annual Symposium on Foundations of Computer Science*, pages 420–428. IEEE, 2013b.
- Dan Garber and Elad Hazan. Faster rates for the frank-wolfe method over strongly-convex sets. In *32nd International Conference on Machine Learning, ICML 2015*, 2015.
- Dan Garber, Shoham Sabach, and Atara Kaplan. Fast generalized conditional gradient method with applications to matrix recovery problems. *arXiv preprint arXiv:1802.05581*, 2018.
- Leon A Gatys, Alexander S Ecker, Matthias Bethge, Aaron Hertzmann, and Eli Shechtman. Controlling perceptual factors in neural style transfer. In *Proceedings of the IEEE Conference on Computer Vision and Pattern Recognition*, pages 3985–3993, 2017.
- Justin Gilmer, Ryan P Adams, Ian Goodfellow, David Andersen, and George E Dahl. Motivating the rules of the game for adversarial example research. *arXiv preprint arXiv:1807.06732*, 2018.
- Ian J Goodfellow, Jonathon Shlens, and Christian Szegedy. Explaining and harnessing adversarial examples. *arXiv preprint arXiv:1412.6572*, 2014.
- Jacques Guélat and Patrice Marcotte. Some comments on Wolfe’s ‘away step’. *Mathematical Programming*, 1986.
- Chuan Guo, Jared S Frank, and Kilian Q Weinberger. Low frequency adversarial perturbation. *arXiv preprint arXiv:1809.08758*, 2018.
- Zaid Harchaoui, Matthijs Douze, Mattis Paulin, Miroslav Dudik, and Jérôme Malick. Large-scale image classification with trace-norm regularization. In *2012 IEEE Conference on Computer Vision and Pattern Recognition*, pages 3386–3393. IEEE, 2012.
- Martin Jaggi. Revisiting frank-wolfe: Projection-free sparse convex optimization. In *Proceedings of the 30th international conference on machine learning*, number CONF, pages 427–435, 2013.
- Martin Jaggi and Marek Sulovský. A simple algorithm for nuclear norm regularized problems. In *ICML*, 2010.
- Thomas Kerdreux and Alexandre d’Aspremont. Frank-wolfe on uniformly convex sets. *arXiv preprint arXiv:2004.11053*, 2020.
- Thomas Kerdreux, Fabian Pedregosa, and Alexandre d’Aspremont. Frank-wolfe with subsampling oracle. *arXiv preprint arXiv:1803.07348*, 2018.
- Simon Lacoste-Julien and Martin Jaggi. An affine invariant linear convergence analysis for frank-wolfe algorithms. *arXiv preprint arXiv:1312.7864*, 2013.
- Simon Lacoste-Julien and Martin Jaggi. On the global linear convergence of Frank–Wolfe optimization variants. In C. Cortes, N. D. Lawrence, D. D. Lee, M. Sugiyama, and R. Garnett, editors, *Advances in Neural Information Processing Systems*, volume 28, pages 496–504. Curran Associates, Inc., 2015.
- Peter Langeberg, Emilio Rafael Balda, Arash Behboodi, and Rudolf Mathar. On the effect of low-rank weights on adversarial robustness of neural networks. *arXiv preprint arXiv:1901.10371*, 2019.

- Jason D Lee, Ben Recht, Nathan Srebro, Joel Tropp, and Russ R Salakhutdinov. Practical large-scale optimization for max-norm regularization. In *Advances in neural information processing systems*, pages 1297–1305, 2010.
- Evgeny S Levitin and Boris T Polyak. Constrained minimization methods. *USSR Computational mathematics and mathematical physics*, 6(5):1–50, 1966.
- Hsueh-Ti Derek Liu, Michael Tao, Chun-Liang Li, Derek Nowrouzezahrai, and Alec Jacobson. Beyond pixel norm-balls: Parametric adversaries using an analytically differentiable renderer. *arXiv preprint arXiv:1808.02651*, 2018.
- Ming Lu, Hao Zhao, Anbang Yao, Feng Xu, Yurong Chen, and Li Zhang. Decoder network over lightweight reconstructed feature for fast semantic style transfer. In *Proceedings of the IEEE International Conference on Computer Vision*, pages 2469–2477, 2017.
- Bo Luo, Yannan Liu, Lingxiao Wei, and Qiang Xu. Towards imperceptible and robust adversarial example attacks against neural networks. In *Thirty-Second AAAI Conference on Artificial Intelligence*, 2018.
- Aleksander Madry, Aleksandar Makelov, Ludwig Schmidt, Dimitris Tsipras, and Adrian Vladu. Towards deep learning models resistant to adversarial attacks. *arXiv preprint arXiv:1706.06083*, 2017.
- Federico Pierucci. *Nonsmooth optimization for statistical learning with structured matrix regularization*. PhD thesis, Université Grenoble Alpes, 2017.
- Ariti Raghunathan, Jacob Steinhardt, and Percy Liang. Certified defenses against adversarial examples. *arXiv preprint arXiv:1801.09344*, 2018a.
- Ariti Raghunathan, Jacob Steinhardt, and Percy S Liang. Semidefinite relaxations for certifying robustness to adversarial examples. In *Advances in Neural Information Processing Systems*, pages 10877–10887, 2018b.
- Scott E Reed, Zeynep Akata, Santosh Mohan, Samuel Tenka, Bernt Schiele, and Honglak Lee. Learning what and where to draw. In *Advances in neural information processing systems*, pages 217–225, 2016.
- Eric Risser, Pierre Wilmot, and Connelly Barnes. Stable and controllable neural texture synthesis and style transfer using histogram losses. *arXiv preprint arXiv:1701.08893*, 2017.
- Ludwig Schmidt, Shibani Santurkar, Dimitris Tsipras, Kunal Talwar, and Aleksander Madry. Adversarially robust generalization requires more data. In *Advances in Neural Information Processing Systems*, pages 5014–5026, 2018.
- Ayon Sen, Xiaojin Zhu, Liam Marshall, and Robert Nowak. Should adversarial attacks use pixel p-norm? *arXiv preprint arXiv:1906.02439*, 2019.
- Shai Shalev-Shwartz, Alon Gonen, and Ohad Shamir. Large-scale convex minimization with a low-rank constraint. *arXiv preprint arXiv:1106.1622*, 2011.
- Mahmood Sharif, Lujo Bauer, and Michael K Reiter. On the suitability of lp-norms for creating and preventing adversarial examples. In *Proceedings of the IEEE Conference on Computer Vision and Pattern Recognition Workshops*, pages 1605–1613, 2018.
- W So. Facial structures of Schatten p-norms. *Linear and Multilinear Algebra*, 27(3):207–212, 1990.
- David Stutz, Matthias Hein, and Bernt Schiele. Disentangling adversarial robustness and generalization. In *Proceedings of the IEEE Conference on Computer Vision and Pattern Recognition*, pages 6976–6987, 2019.

- Ryota Tomioka and Taiji Suzuki. Convex tensor decomposition via structured Schatten norm regularization. In *Advances in neural information processing systems*, pages 1331–1339, 2013.
- Eric Wong and J Zico Kolter. Provable defenses against adversarial examples via the convex outer adversarial polytope. *arXiv preprint arXiv:1711.00851*, 2017.
- Eric Wong, Frank R Schmidt, and J Zico Kolter. Wasserstein adversarial examples via projected sinkhorn iterations. *arXiv preprint arXiv:1902.07906*, 2019.
- Kaidi Xu, Sijia Liu, Pu Zhao, Pin-Yu Chen, Huan Zhang, Quanfu Fan, Deniz Erdogmus, Yanzhi Wang, and Xue Lin. Structured adversarial attack: Towards general implementation and better interpretability. *arXiv preprint arXiv:1808.01664*, 2018.
- Ziang Yan, Yiwen Guo, and Changshui Zhang. Subspace attack: Exploiting promising subspaces for query-efficient black-box attacks, 2019.
- Yuzhe Yang, Guo Zhang, Dina Katabi, and Zhi Xu. Me-net: Towards effective adversarial robustness with matrix estimation. *arXiv preprint arXiv:1905.11971*, 2019.

A More on structured norms

In [Amini et al., 2017, §2.3.] introduce $\Sigma_{\mathcal{G}}$ a 1-group- p -Schatten norms where the group can overlaps. In this case also it is possible to access the LMO leveraging on the knowledge of the dual norm $\Sigma_{\mathcal{G}}$

$$\Sigma_{\mathcal{G}}^{\circ}(M) = \max_{g \in \mathcal{G}} \|M[g]\|_{S(q)},$$

where $S(q)$ with $1/p + 1/q = 1$.

From [Pierucci, 2017, (2.5),(2.6)] shows that the group-nuclear norms $\|\cdot\|_{\mathcal{G},1,S(1)}$ are convex surrogates of some group-rank function and as such enforce solution that are low-rank on some groups.

We stated the LMO q -Schatten for $q = 1$, which corresponds to the trace-norm or nuclear norm, and $q \in]1, +\infty[$ separately. The LMO for the Schatten norm with $q = +\infty$ is given by

$$\text{LMO}_{\|\cdot\|_{S(\infty)} \leq \rho} \triangleq \rho UV^T,$$

where $M = USV^T$ with U and V the matrix of left and right normalized singular vectors.

So far we only considered sparsity (at the group level) inducing group-norm, but more general norms can be simply written with $r \in]1, +\infty[$ and $p \in [1, +\infty[$

$$\|x\|_{\mathcal{G},r,S(p)} = \left(\sum_{g \in \mathcal{G}} \|x[g]\|_{S(p)}^r \right)^{1/r},$$

however, sparsity of the global adversarial perturbation is something which is not interesting to loose as it concentrates the perturbation only on some areas.

B More on numerical results

Table 4: MNIST and CIFAR-10 extensive white-box attack results against standardly trained models. FWnucl 20*: FWnucl with $\epsilon = 1$. FWnucl 20+: FWnucl with $\epsilon = 3$.

Network	Clean	Accuracy under attack				
		FWnucl 20*	FWnucl 20+	PGDnucl 20	PGD 20	FGSM
MNIST						
LeNET	99.32	93.82	36.24	98.01	0.25	38.62
SmallCNN	99.47	94.21	76.9	97.32	20.02	90.63
CIFAR-10						
ResNet-18	93.94	2.77	0.00	24.22	0.00	18.60
WideResNet	95.28	3.65	0.00	25.18	0.00	26.86
ResNet-50	93.22	2.99	0.00	19.35	0.00	22.26

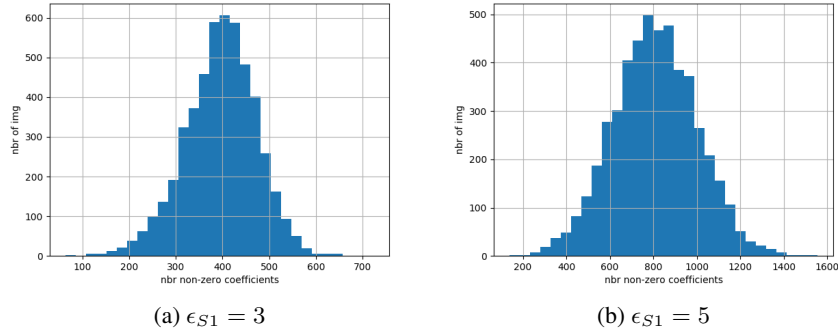


Figure 8: Showing the distribution of number of modified pixels between a CIFAR10 test image with integer pixel values in $[0, 255]$ and a perturbed image in the same format. We use 5000 images in CIFAR10 test set. Each image is perturbed via adding $\epsilon_{S_1} uv^T$ to the normalized initial test image and then by unnormalizing and clamping it to integers values between $[0, 255]$. u and v are the right and left singular vectors associated to the largest singular value. In Frank-Wolfe nuclear the Frank-Wolfe vertex that are added to the perturbation are of the form of $\epsilon_{S_1} uv^T$ where (u, v) are singular-vectors associated to the largest singular value of the perturbed image along the iterations.

Table 5: MNIST and CIFAR-10 extensive white-box attack results with $\epsilon_{S_1} = 5$.

Network	Training Model	Accuracy under attack			
		FWnucl 10	FWnucl 20	FWnucl 50	FWnucl 100
MNIST					
LeNET	Madry	92.67	90.39	87.84	86.61
	ME-NET	50.60	39.02	30.12	26.65
SmallCNN	Madry	96.34	94.5	92.17	91.02
	ME-NET	63.75	60.98	55.98	54.65
CIFAR-10					
ResNet-18	Madry	0.74	0.19	0.04	0.01
	ME-NET	3.21	0.80	0.29	0.10
WideResNet	Madry	0.81	0.19	0.03	0.02
	ME-NET	14.19	8.32	4.42	3.29
ResNet-50	Madry	1.09	0.25	0.06	0.03
	ME-NET	16.40	9.17	4.28	2.89

Table 6: Comparison of the white-box attacks for MNIST on SmallCNN adversarially trained. PGD, on the ℓ_∞ ball, and FGSM have a total perturbation scale of 76.5/255(0.3), and step size 2.55/255(0.01). PGD runs for 20 iterations.

Attack	LeNet		SmallCNN	
	Mean ℓ_2	Mean $\ \cdot\ _{S_2}$	Mean ℓ_2	Mean $\ \cdot\ _{S_2}$
FWnucl 20 ($\epsilon_{S_1} = 1$)	0.45	0.75	0.45	0.80
FWnucl 20 ($\epsilon_{S_1} = 3$)	0.93	1.91	1.00	2.14
PGD 20	3.87	16.12	4.67	18.98
FGSM	6.15	24.92	3.57	12.17

Table 7: Fooling rates of FWnucl adversarial perturbations between several models for CIFAR-10 test set. The row indicates the source models on which adversarial examples are grafted and the column indicates the target model on which these attacks are evaluated. These models are not adversarially trained. FWnucl run for 20 iterations with $\epsilon_{S_1} = 5$.

	ResNet-18	DenseNet121	GoogLeNet
ResNet-18	97.48	86.00	84.64
DenseNet121	91.31	98.36	90.45
GoogLeNet	83.55	86.03	98.37

Table 9: MNIST and CIFAR-10 extensive white-box attack results with random initialization. FWnucl 20*: FWnucl with $\epsilon = 1$. FWnucl 20+: FWnucl with $\epsilon = 3$.

Network	Training Model	Clean	Accuracy under attack				
			FWnucl 20*	FWnucl 20+	PGD 20	FGSM	CW
MNIST							
LeNET	Madry	98.38	95.00	85.37	95.79	96.59	98.38
	ME-NET	99.24	97.02	52.63	74.88	46.18	99.00
SmallCNN	Madry	99.12	98.03	92.35	95.77	97.95	99.12
	ME-NET	99.42	89.04	71.75	76.84	54.09	91.44
CIFAR-10							
ResNet-18	Madry	81.25	34.64	0.45	49.95	55.91	78.61
	ME-NET	92.09	29.66	4.01	4.99	44.80	79.57
WideResNet	Madry	85.1	32.3	0.33	52.49	59.06	82.69
	ME-NET	92.09	24.16	4.07	12.73	59.33	80.89
ResNet-50	Madry	87.03	29.24	0.31	53.01	61.44	84.72
	ME-NET	92.09	28.49	4.09	9.14	58.51	83.21

Table 8: Comparisons of the attacks for projected gradient descent with nuclear norm (PGDnucl). MNIST and CIFAR-10 extensive white-box attack results for PGDnucl. PGDnucl 20*: PGDnucl 20 with $\epsilon_{S1} = 1$; PGDnucl 20+: PGDnucl 20 with $\epsilon_{S1} = 3$; PGDnucl 20#: PGDnucl 20 with $\epsilon_{S1} = 5$

Network	Training Model	Accuracy under attack		
		PGDnucl 20*	PGDnucl 20+	PGDnucl 20#
MNIST				
LeNET	Madry	95.36	87.48	69.50
	ME-NET	98.21	97.83	94.78
SmallCNN	Madry	98.15	93.20	80.51
	ME-NET	88.35	85.33	76.23
CIFAR-10				
ResNet-18	Madry	78.38	74.46	58.57
	ME-NET	87.21	76.28	58.58
WideResNet	Madry	81.49	76.38	–
	ME-NET	89.08	74.74	54.37
ResNet-50	Madry	82.87	77.19	60.68
	ME-NET	87.26	78.29	62.90

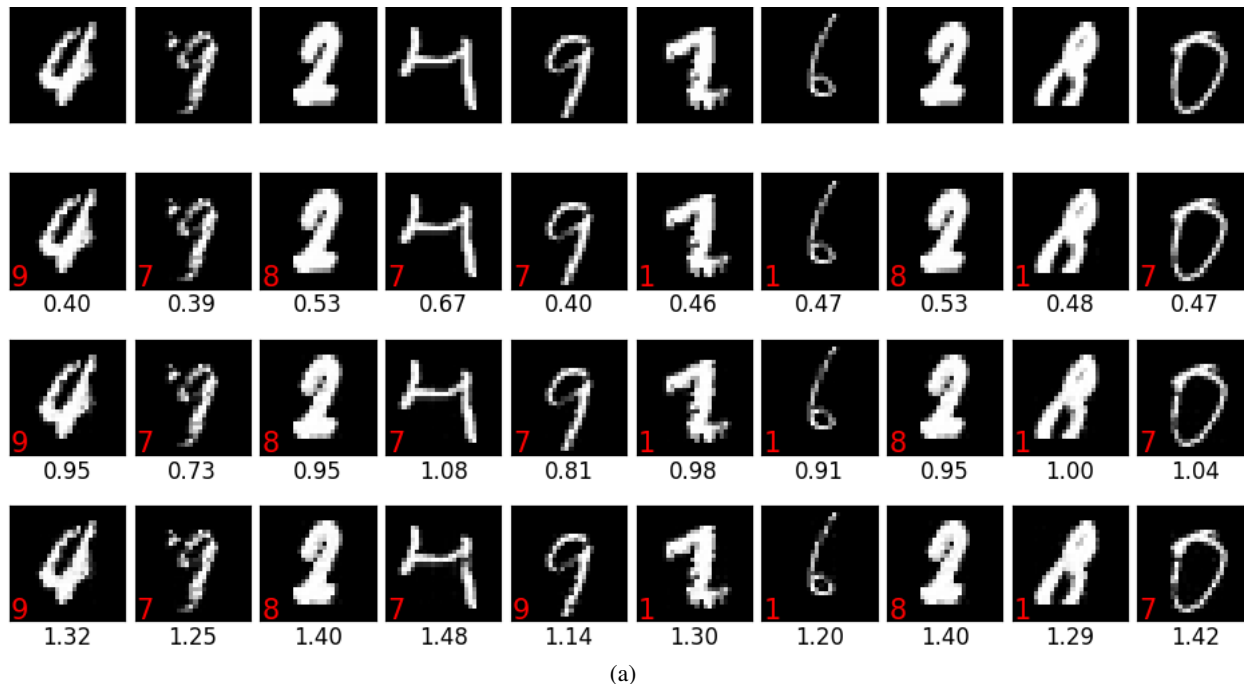
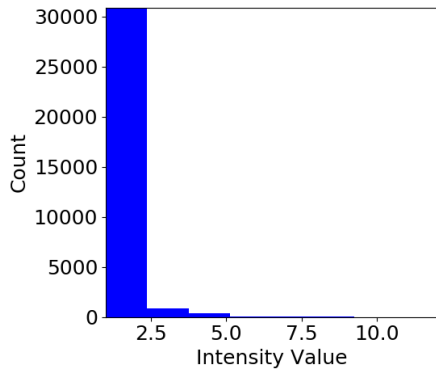
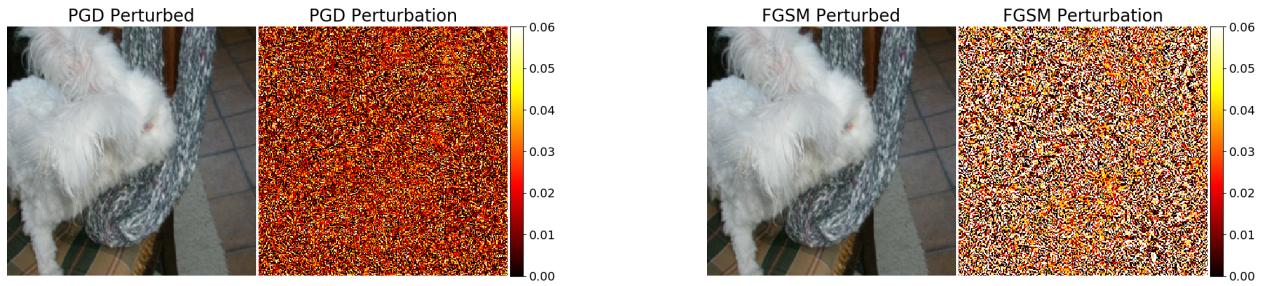
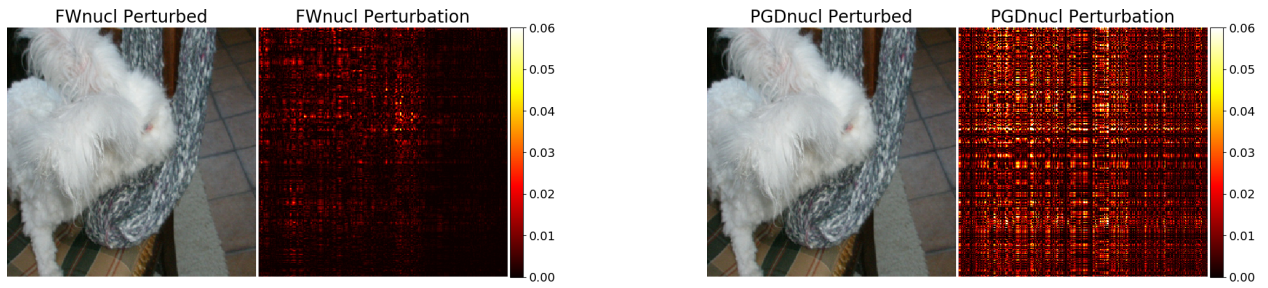


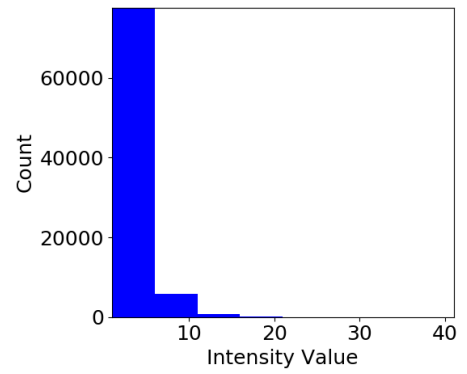
Figure 9: FWnucl adversarial examples for the MNIST dataset for different radii, (a) original images (first row), adversarial example generated by (b) FWnucl with $\epsilon_{S1} = 1$ (second row), (c) FWnucl with $\epsilon_{S1} = 3$ (third row) and (d) FWnucl with $\epsilon_{S1} = 5$ (third row). The fooling label is shown on the image.



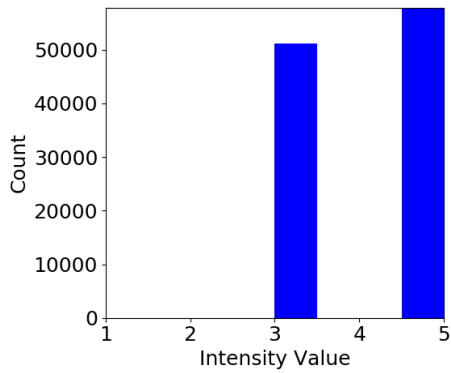
Figure 10: Adversarial examples on MNIST dataset against the Madry defense (a) original images (first row), adversarial examples generated by (b) FWnucl (second row), (c) PGDnucl (third row), (d) PGD (fourth row) and (e) FGSM (fifth row); the fooling label is shown on bottom-right of each image, and the l_2 norm of adversarial noise is written below each image.



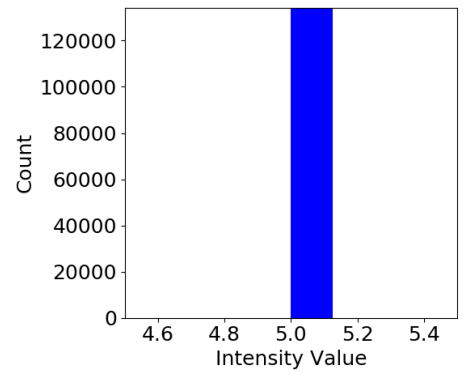
(a) FWnucl



(b) PGDnucl



(c) PGD



(d) FGSM

Figure 11: ResNet-50 adversarial examples with the histogram of non-zero pixel intensities corresponding to the attack perturbations for the **Angora** original image label.

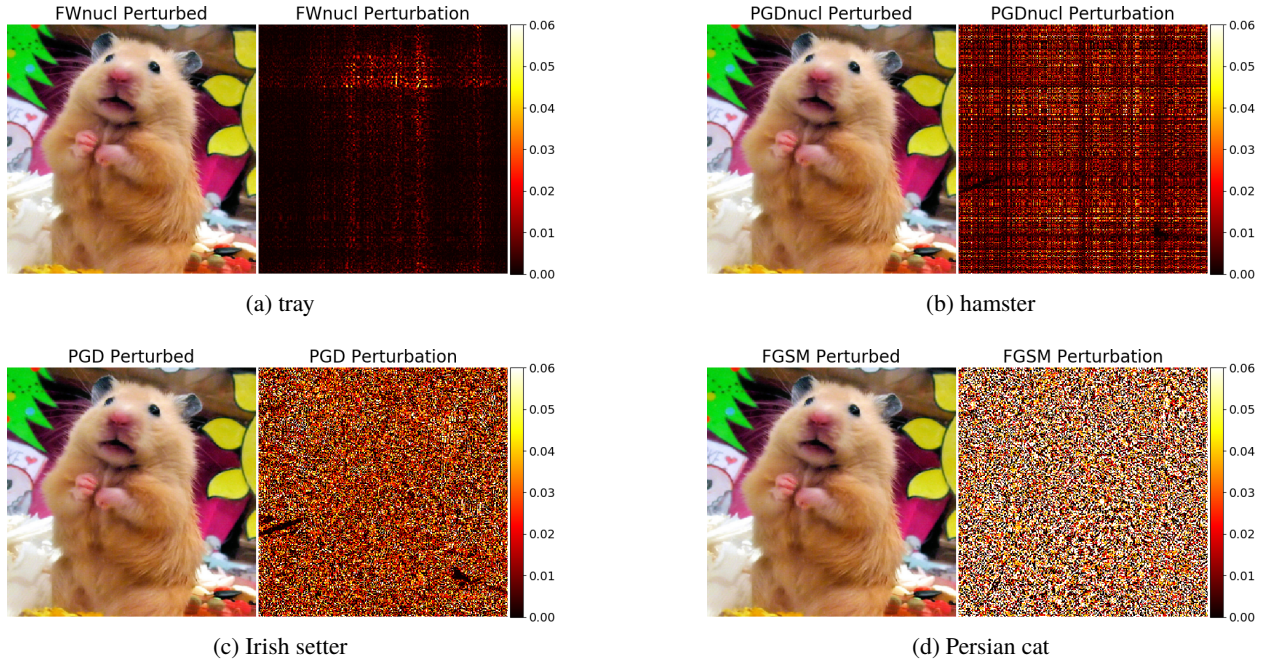


Figure 12: ResNet-50 adversarial examples with the heat map of pixel intensities corresponding to the attack perturbations for the original image with the label **hamster**.

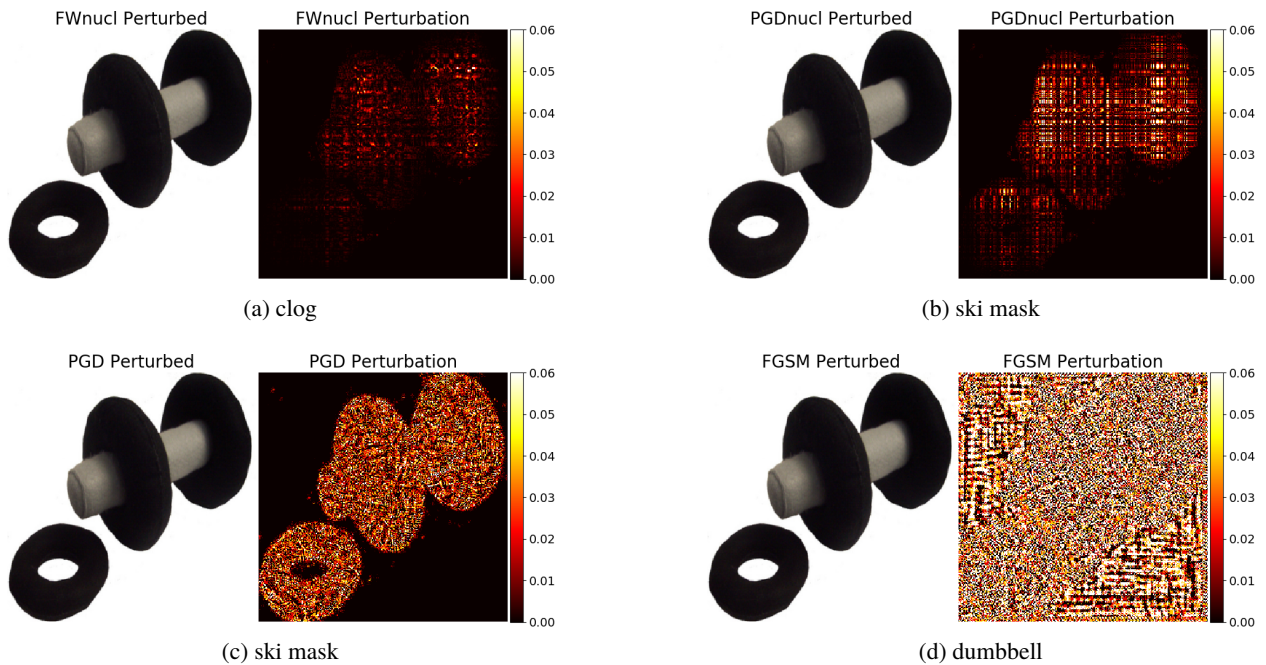


Figure 13: ResNet-50 adversarial examples with the heat map of pixel intensities corresponding to the attack perturbations for the original image with the label **dumbbell**.

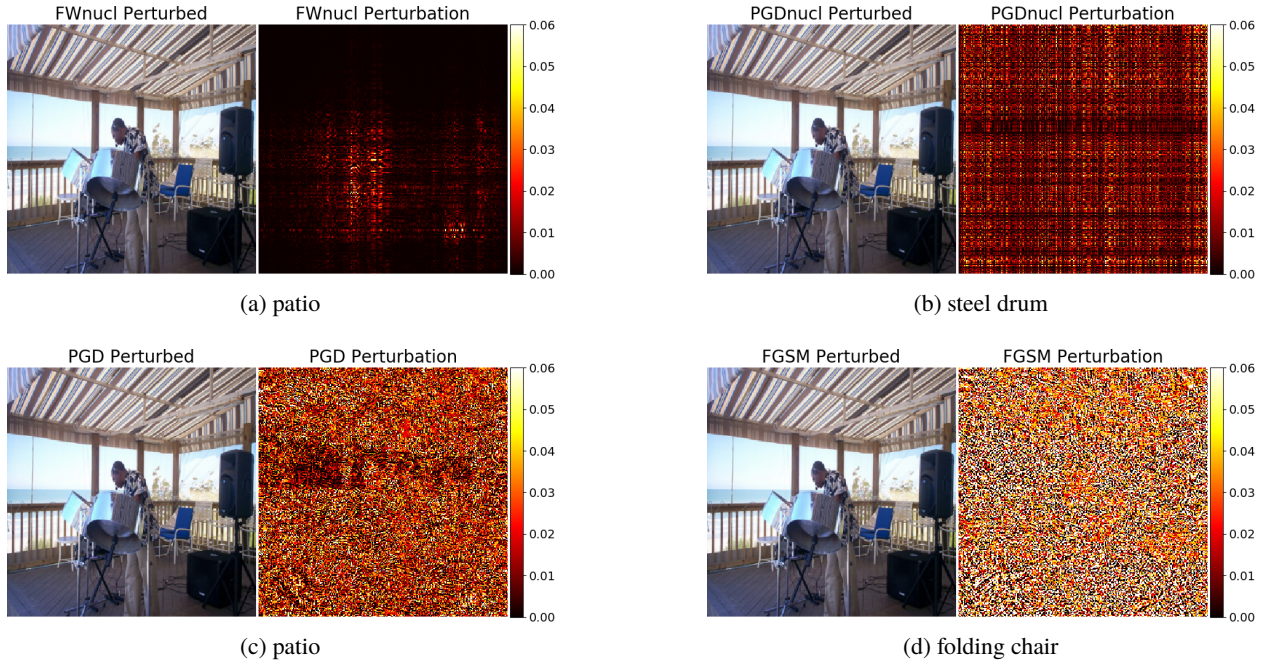


Figure 14: ResNet-50 adversarial examples with the heat map of pixel intensities corresponding to the attack perturbations for the original image with the label **steel drum**.

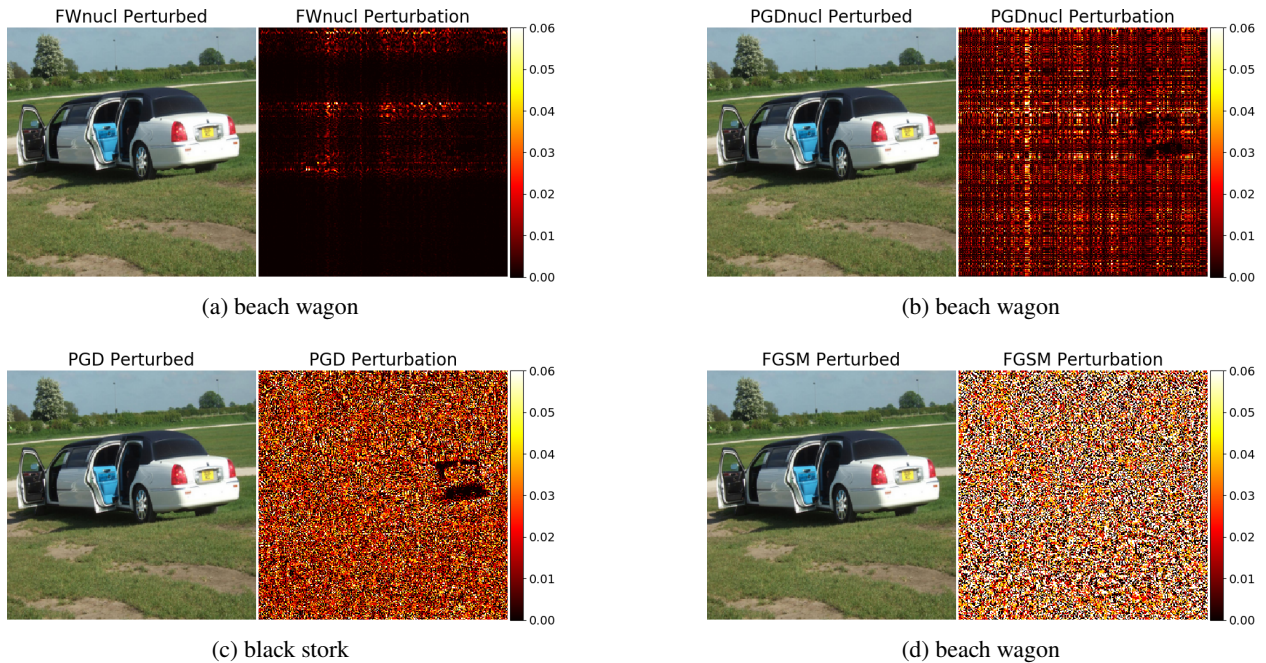


Figure 15: ResNet-50 adversarial examples with the heat map of pixel intensities corresponding to the attack perturbations for the original image with the label **limousine**.

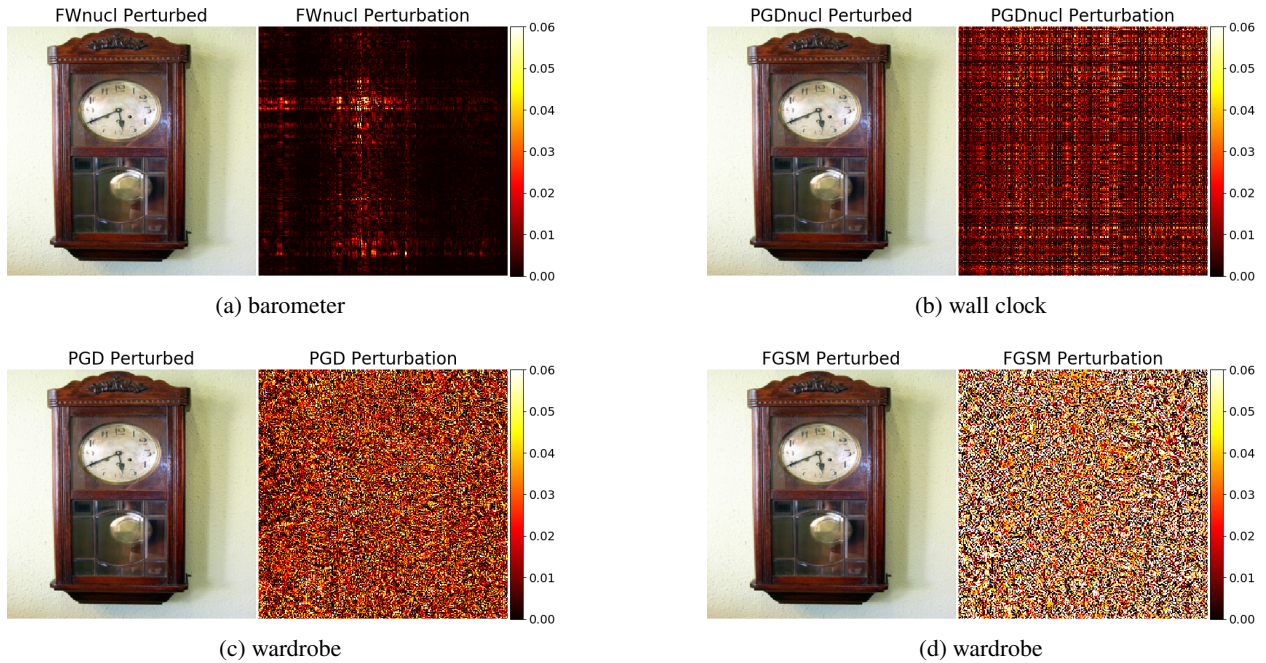


Figure 16: ResNet-50 adversarial examples with the heat map of pixel intensities corresponding to the attack perturbations for the original image with the label **wall clock**.

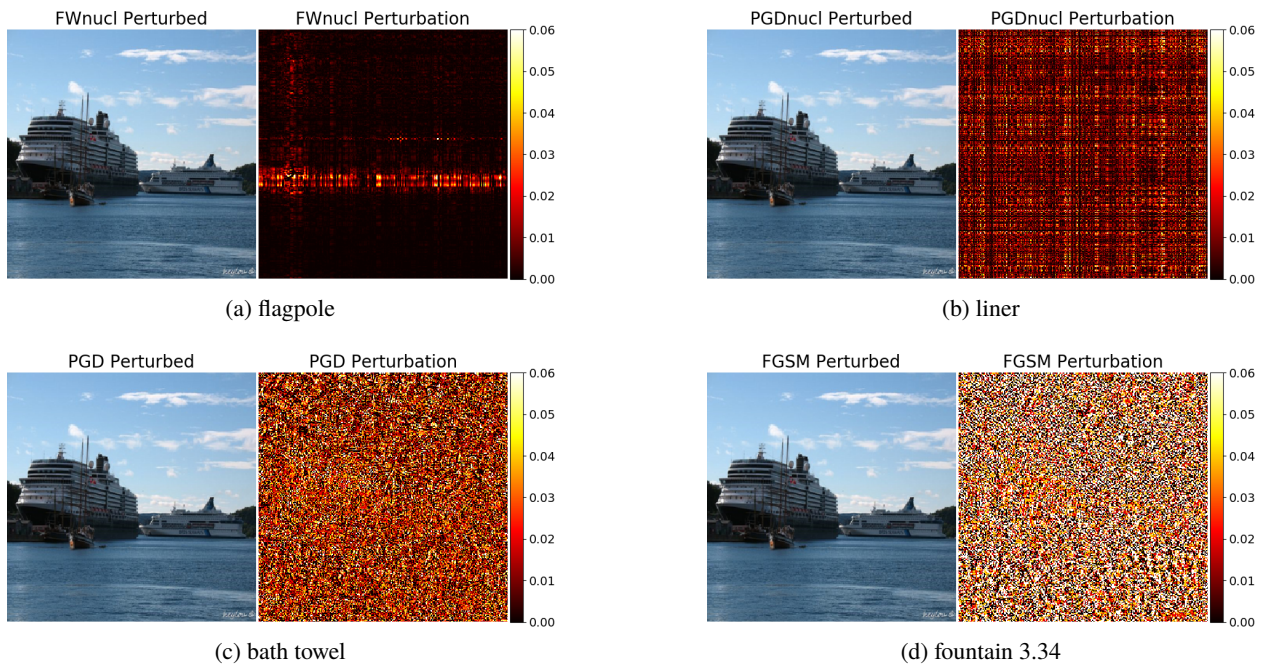


Figure 17: ResNet-50 adversarial examples with the heat map of pixel intensities corresponding to the attack perturbations for the original image with the label **liner**.

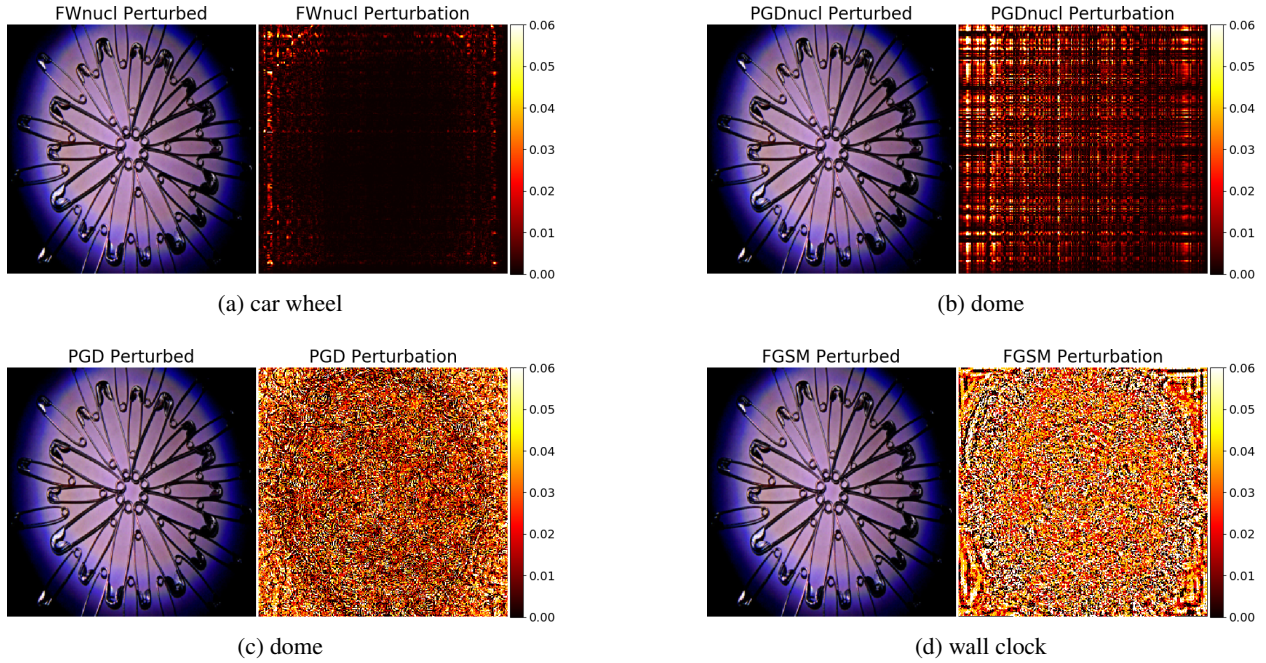


Figure 18: DenseNet121 adversarial examples with the heat map of pixel intensities corresponding to the attack perturbations for the original image with the label **safety pin**.

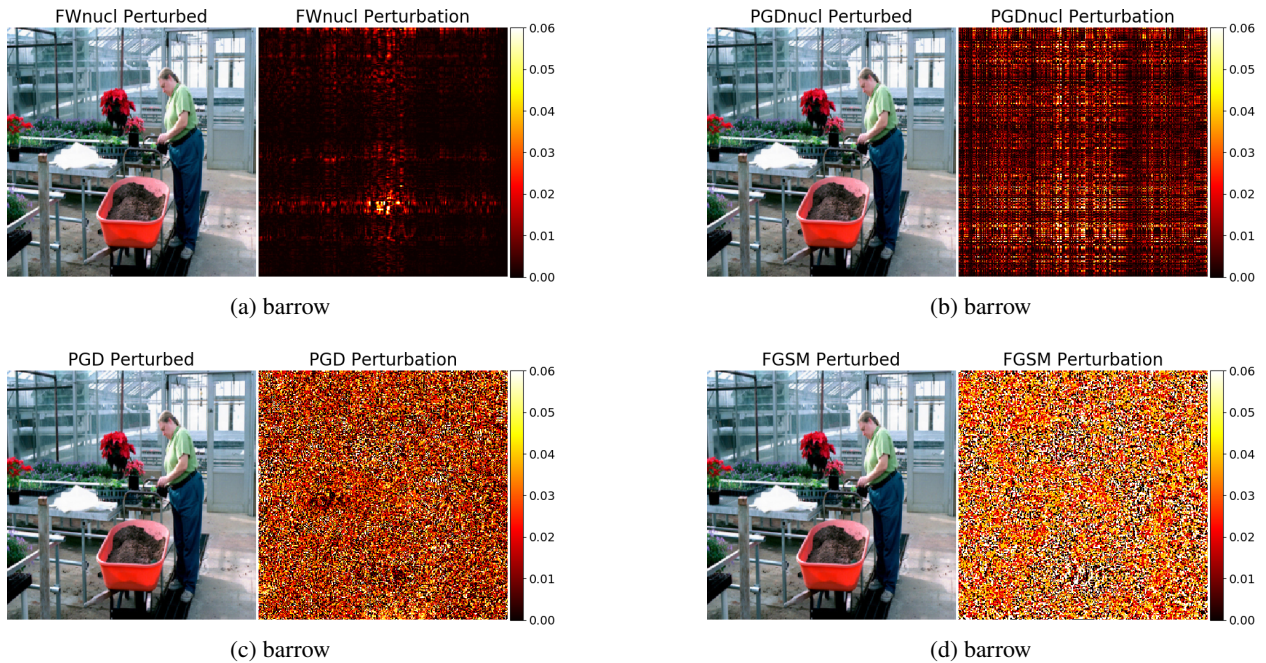


Figure 19: DenseNet121 adversarial examples with the heat map of pixel intensities corresponding to the attack perturbations for the original image with the label **greenhouse**.

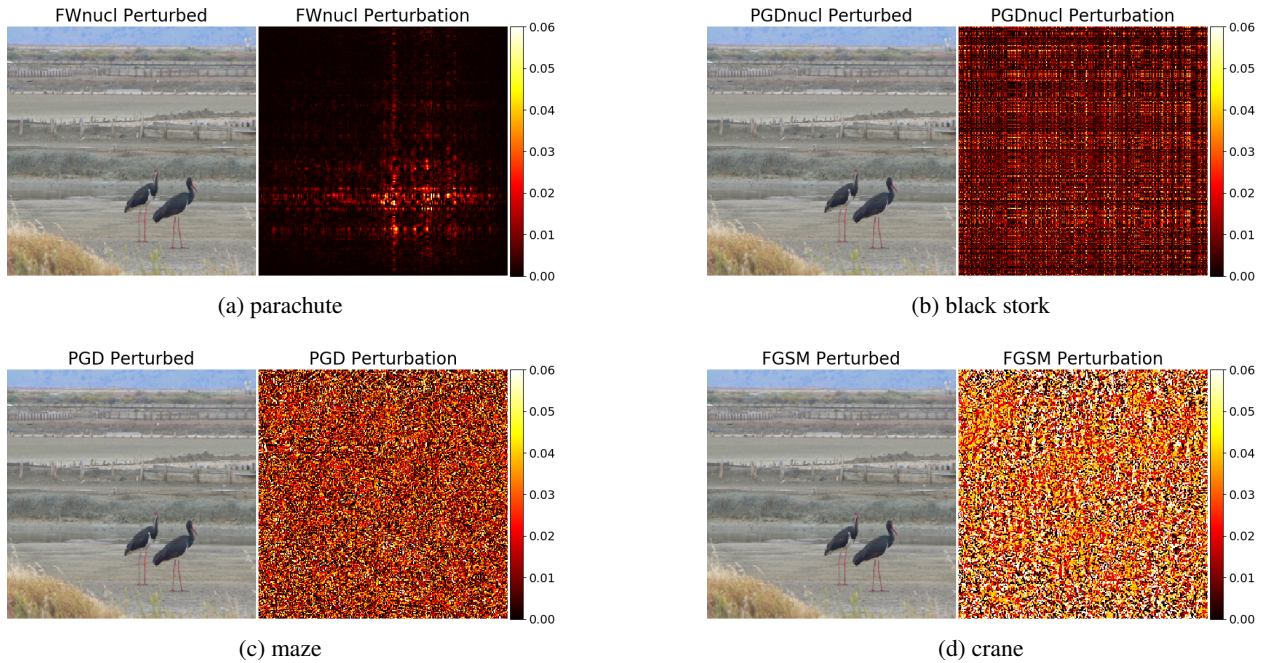


Figure 20: DenseNet121 adversarial examples with the heat map of pixel intensities corresponding to the attack perturbations for the original image with the label **black stork**.

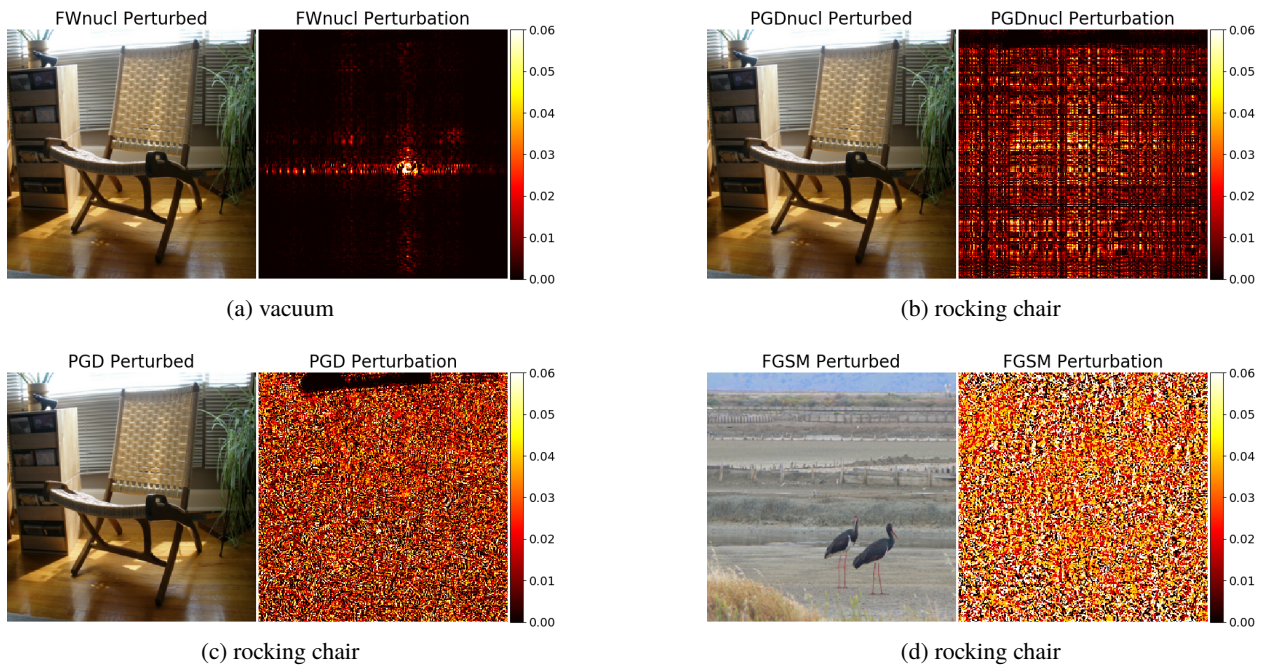


Figure 21: DenseNet121 adversarial examples with the heat map of pixel intensities corresponding to the attack perturbations for the original image with the label **folding chair**.

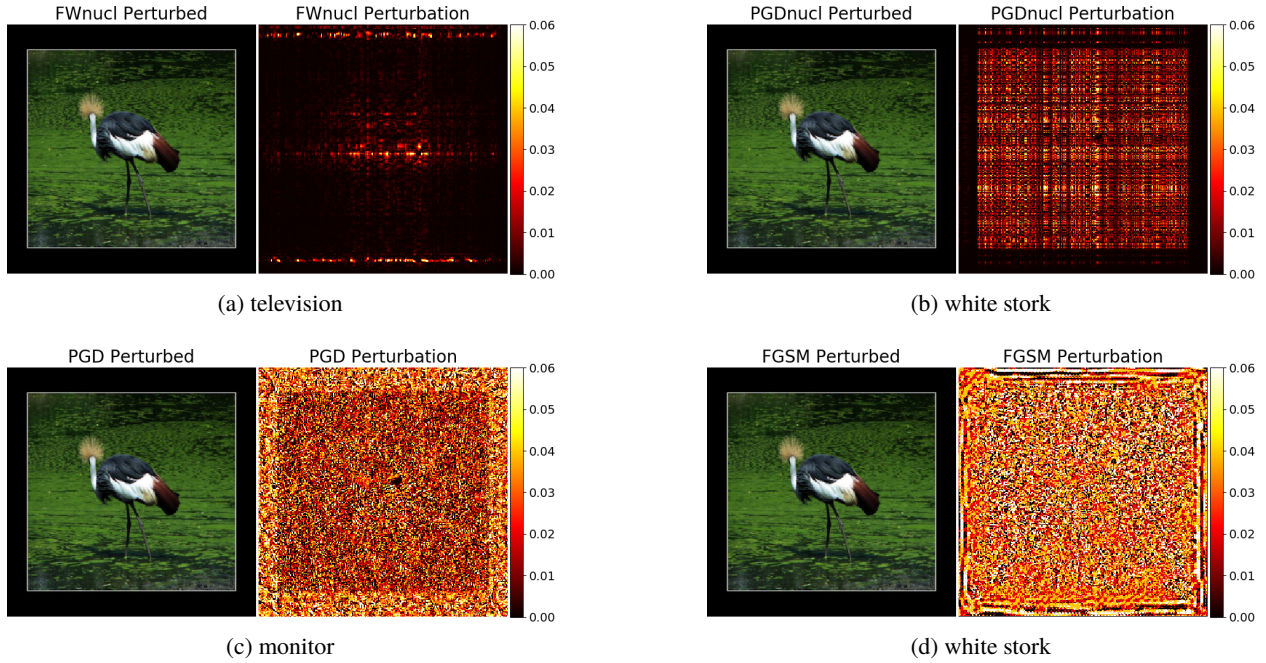


Figure 22: DenseNet121 adversarial examples with the heat map of pixel intensities corresponding to the attack perturbations for the original image with the label **crane**.

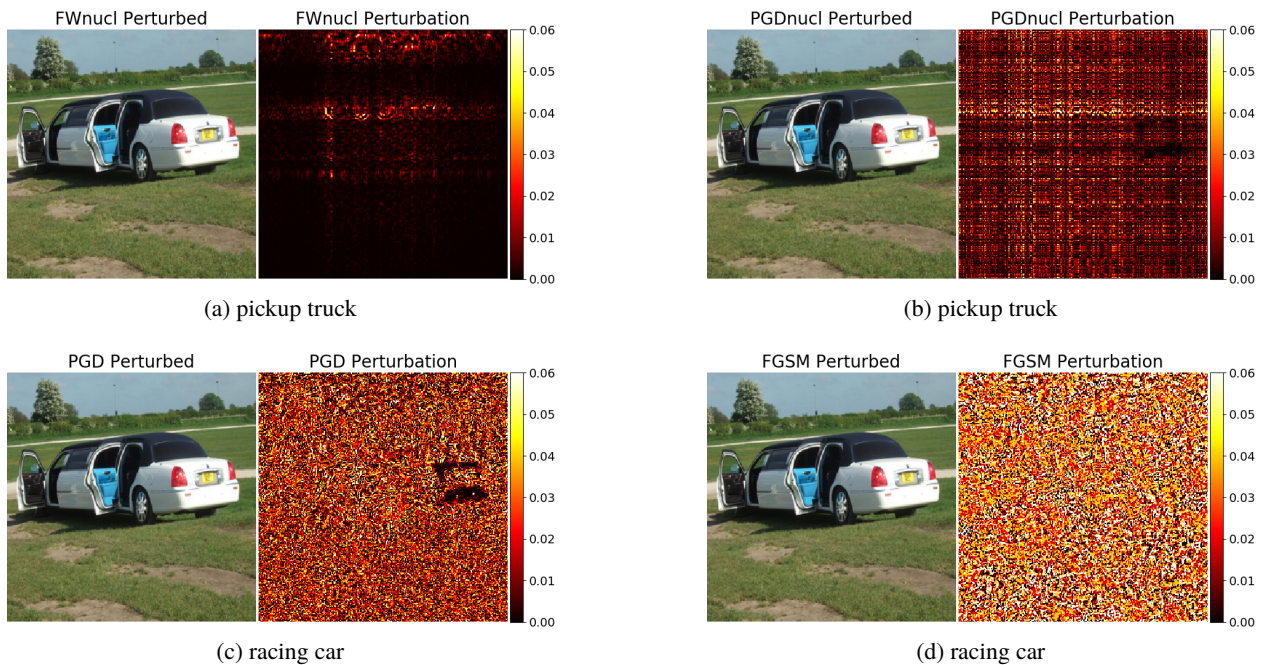


Figure 23: DenseNet121 adversarial examples with the heat map of pixel intensities corresponding to the attack perturbations for the original image with the label **limousine**.

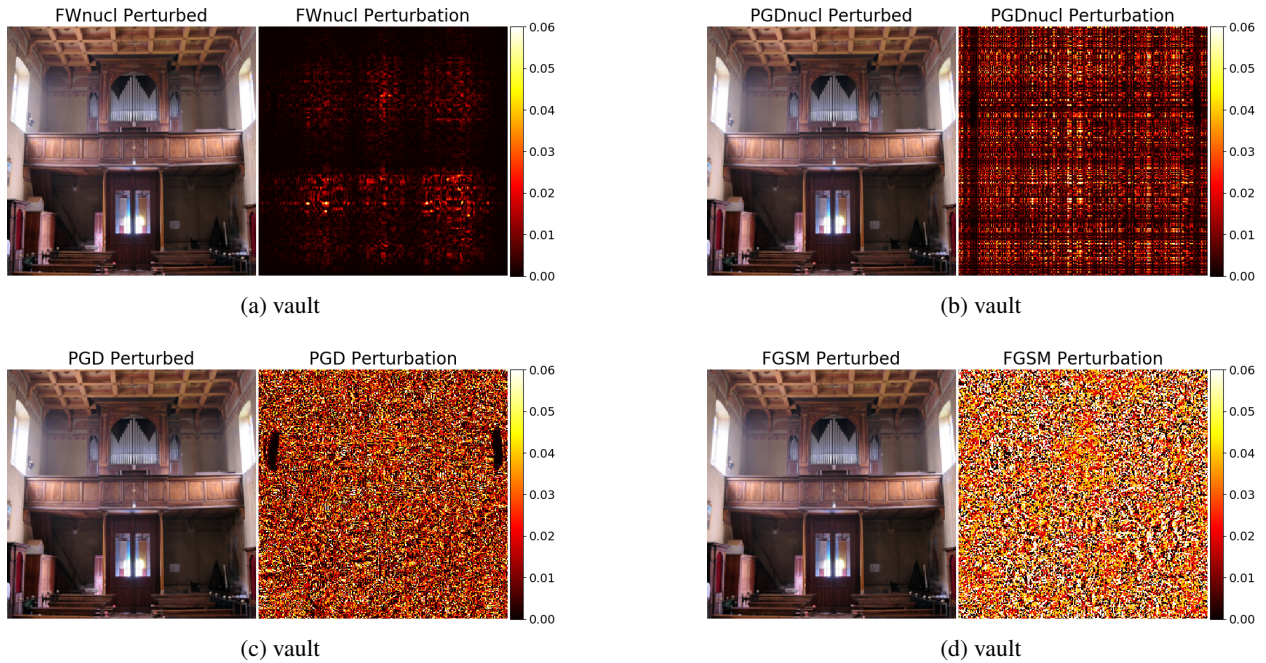


Figure 24: DenseNet121 adversarial examples with the heat map of pixel intensities corresponding to the attack perturbations for the original image with the label **organ**.

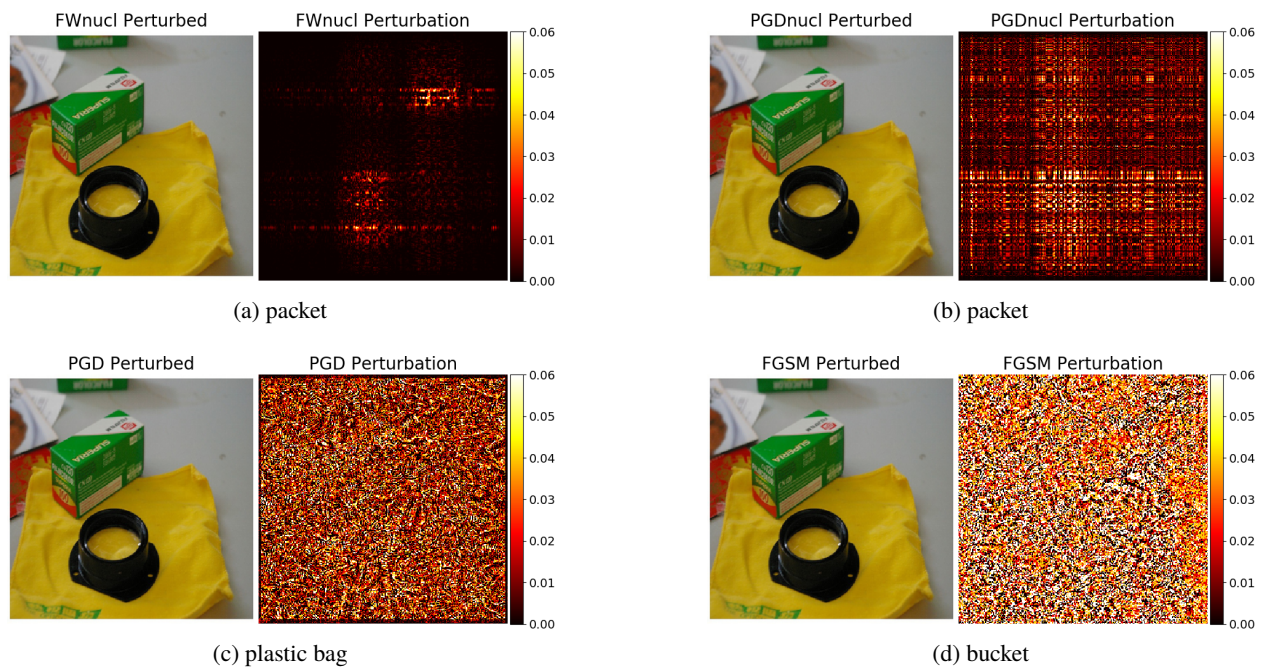


Figure 25: DenseNet121 adversarial examples with the heat map of pixel intensities corresponding to the attack perturbations for the original image with the label **loupe**.

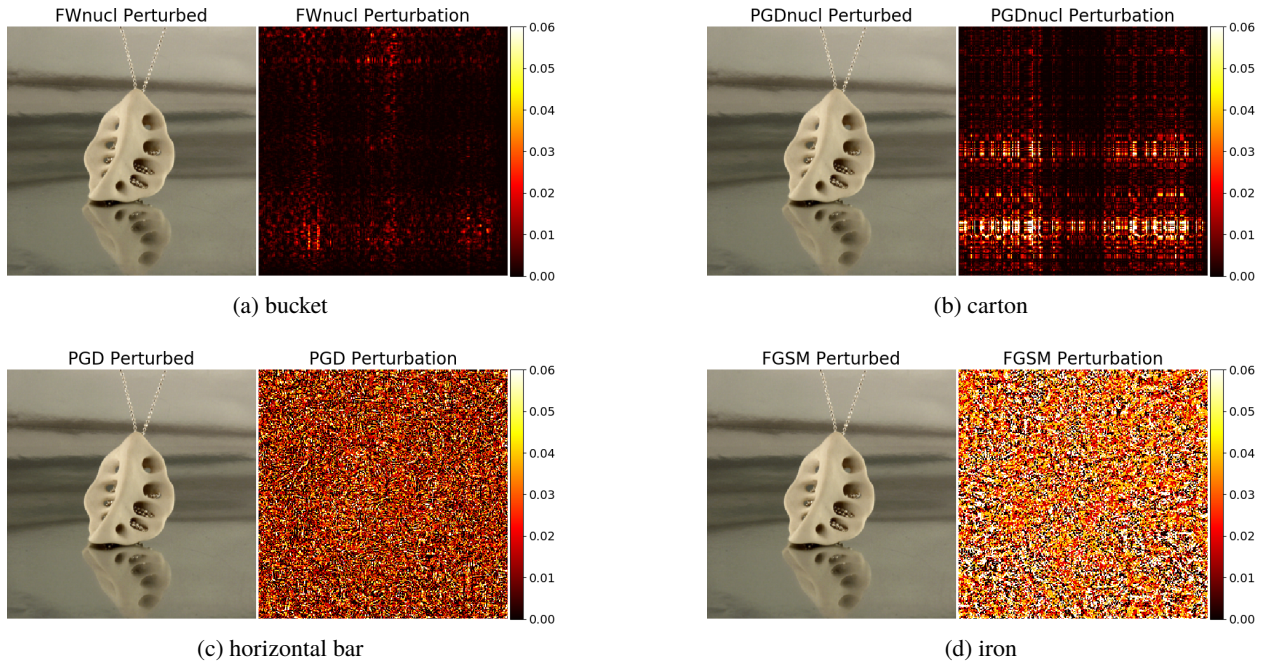


Figure 26: DenseNet121 adversarial examples with the heat map of pixel intensities corresponding to the attack perturbations for the original image with the label **necklace**.

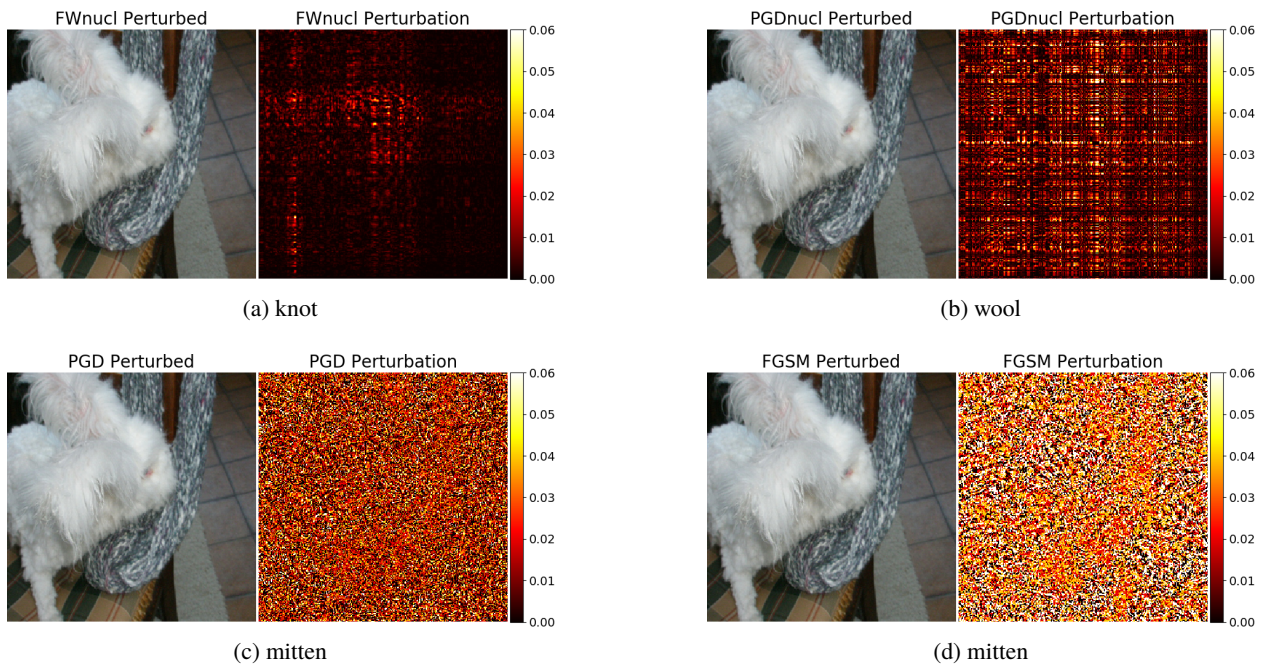


Figure 27: DenseNet121 adversarial examples with the heat map of pixel intensities corresponding to the attack perturbations for the original image with the label **Angora**.

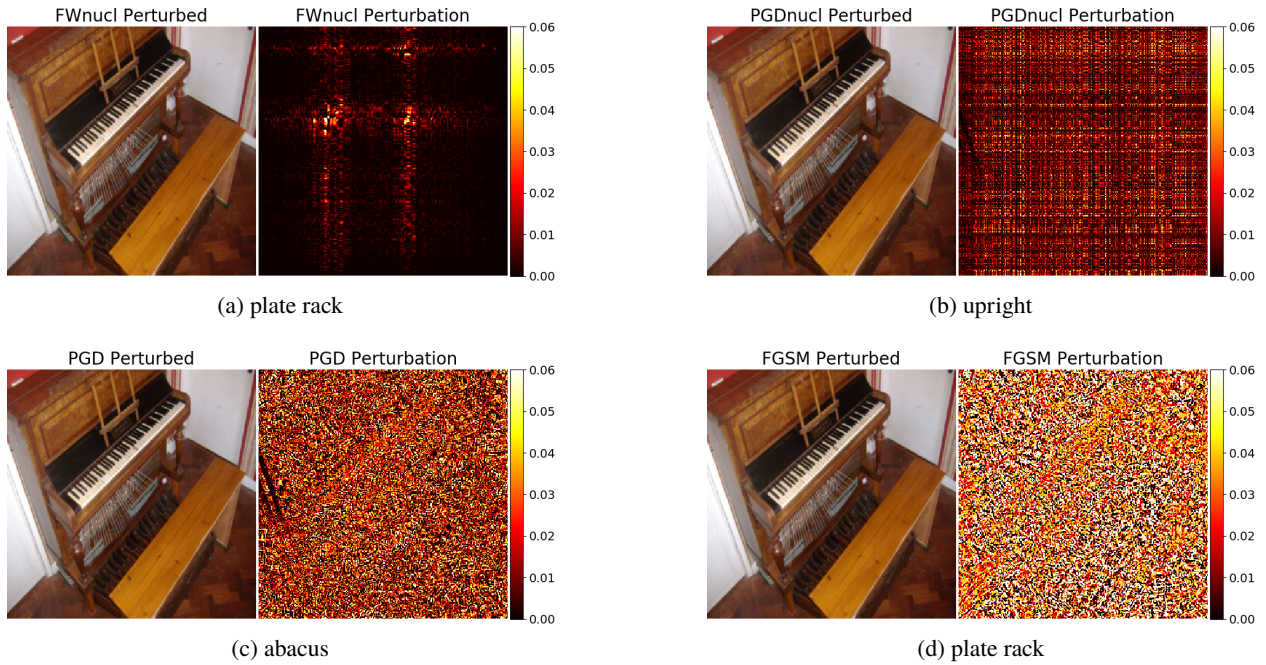


Figure 28: DenseNet121 adversarial examples with the heat map of pixel intensities corresponding to the attack perturbations for the original image with the label **upright**.

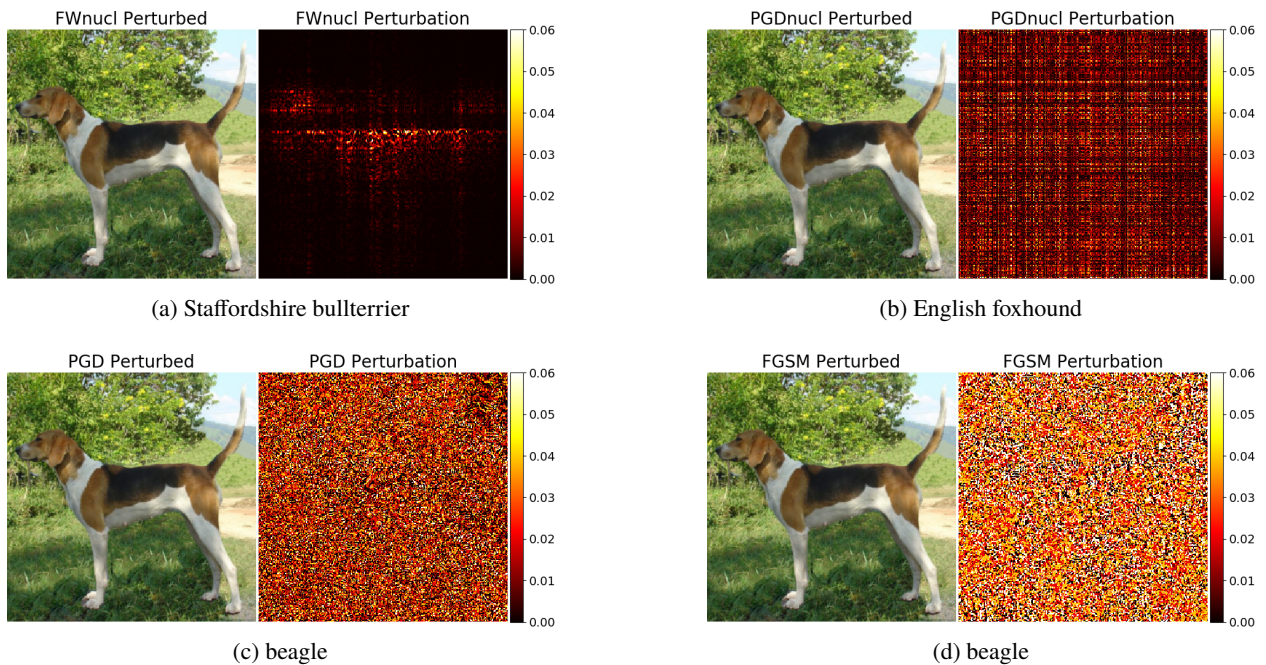


Figure 29: DenseNet121 adversarial examples with the heat map of pixel intensities corresponding to the attack perturbations for the original image with the label **English foxhound**.